Nonlinear Dyn (2025) 113:20687–20710
https://doi.org/10.1007/s11071-025-11236-7

RESEARCH

Frequency analysis of dynamic systems loaded by both parametric and external excitations, with application to rotor dynamics

Alessandro De Felice · Silvio Sorrentino

Received: 3 November 2024 / Accepted: 9 April 2025 / Published online: 6 June 2025

Abstract The analysis of critical conditions of dynamic systems under combined parametric and external excitations is a research field of theoretical interest with important applications in several branches of physics and engineering. Parametric excitation occurs in the presence of time-varying coefficients in the dynamic equilibrium equations, and an extensive body of literature exists in the case of time-periodic coefficients. Dynamic systems under the effects of both parametric and external excitations are worthy of great attention as well, since they represent a rather common occurrence. This study is focused on the development of a theoretical method of analysis of general validity, however applied to rotor dynamics. Parametrically excited rotors constitute a research field in which theoretical developments are still needed to fully understand problems of practical relevance such as instability and resonant behaviour, which can cause issues ranging from anomalous noise and wear to catastrophic failures in several classes of machines. The additional effect of unbalance (always present in real rotors) causes external harmonic loads acting on flexural deflection, which can affect the dynamic responses of the machines in their stable operational fields. The aim of this study, therefore, is the frequency analysis of dynamic systems under the effects of both parametric and external excitations in stable working conditions. Basic models of distributed-parameter slender rotors are considered to facilitate decoupling of the equations of motion, and the analysis of steady-state responses, including both cases in which natural frequencies are independent of, and dependent on, angular speed, the latter case due to gyroscopic effect. Steady-state responses are studied by reducing the problem to the analysis of non-homogeneous single-degree-of-freedom damped Mathieu-Hill equations. It is shown that, even in the linear problem, a theoretically infinite sequence of resonances is related to each modal coordinate of the decoupled system, due to the combination of parametric and external excitation frequencies, and that, in the presence of parametric excitation, flexural critical speeds can occur at lower values than in the same, non-parametrically excited rotors.

Keywords Parametric excitation · Non-homogeneous Mathieu-Hill equation · Floquet analysis · Stability · Rotor dynamics · Unbalance · Frequency analysis · Resonance · Critical speed

A. De Felice · S. Sorrentino (✉)
Department of Engineering Enzo Ferrari, University of Modena and Reggio Emilia, Modena, Italy
e-mail: silvio.sorrentino@unimore.it

A. De Felice
e-mail: alessandro.defelice@unimore.it

1 Introduction

The analysis of dynamic systems under combined parametric and external excitations is a research field of both theoretical and practical importance. Early studies on forced oscillations of Mathieu-Hill equations [1] were motivated by experimental evidence in electrical circuits [2], eventually leading to the mathematical derivation of the steady-state solution as proposed by H. D'Angelo in 1970 [3]. Other important studies on time-varying coefficient differential systems dedicated marginal attention to this problem [4], and the results obtained in [3], still reported in [5] (even though not reproducing correctly the demonstration), were then partially forgotten. Several more recent studies ignored the solution presented in [3], as [6, 7], in some cases focusing on some specific mathematical aspects of the problem, as for instance the existence of periodic solutions for a forced Hill equation [8, 9], the oscillatory nature of the solution of a particular example of forced Mathieu equation [10], or the existence of periodic and subharmonic solutions of a non-homogeneous Hill equation [11]. While in [12] some partial insights into the problem were obtained by following a different approach, based on an energy-rate method applied to detect the so-called 'splitting curves', consisting of periodic solution curves embedded in stable or unstable regions of the stability map, or Ince-Strutt diagram, of the Mathieu equation [13].

As for applications, an extended body of literature exists focused on stability analysis of parametrically excited systems, also including external excitation. On the other hand, frequency analysis of dynamic systems under the effects of both parametric and external excitations in stable working conditions, at least in the mechanical engineering field, received less attention [6].

In this study, mainly theoretical, a frequency domain analysis method based on the result derived in [3] is proposed, with application to rotor dynamics, i.e. to rotating machines under combined parametric and external excitations.

The analysis of parametrically excited rotors is in itself a research field in which developments in theoretical investigations are still needed to fully understand problems of practical relevance. Among the most important applications, slender rotors loaded by periodic axial end thrusts can be mentioned, with possible unstable flexural behaviour at excitation amplitudes far below the static critical buckling load [14–16]. High-speed and high-power-transmitting rotors, commonly used in turbines and compressors for power plant and aeronautical applications, slender shafts and multi-bladed rotors in helicopters [17, 18], as well as hydraulically actuated clutch systems in automotive drivelines [19], represent other important examples of rotor systems which can be affected by issues caused by parametric excitation.

The main sources of parametric excitation in rotors are either anisotropy in their rotating elements, with excitation frequency proportional to angular speed [20, 21], also including the effects of cracks [22, 23], or oscillating components of external loads, as axial end thrust and twisting moment, with excitation frequency that can be independent with respect to angular speed [24].

Several studies focused on stability analysis of parametrically excited rotors, considering as causes of instability: *i*) anisotropy in the rotating elements of the machine [21], or in both its rotating and non-rotating elements, including the effects of cracks (which in horizontal rotating shafts may cause instability of the system because of the periodic opening and closing of the crack, a 'breathing mechanism' causing stiffness variation and parametric excitation of the rotor [23, 25, 26]); in these studies the adopted models range from the Jeffcott rotor [27, 28] to 3D finite element models [23, 29, 30,]; *ii*) oscillating components of external loads, including lumped-parameter models [31], and distributed-parameter models such as axially loaded spinning Rayleigh beams [32], Timoshenko beams [33], rotating flexible shafts driven by oscillating applied torques [34], Timoshenko spinning beams carrying rigid discs, loaded by axial end thrusts and twisting moments [35, 36].

However, none of the above-mentioned studies focused on frequency analysis of rotor systems in stable working conditions, under the effects of both parametric and external excitations (unbalance, always present in real rotors). Even though unbalance does not move the linear stability threshold due to parametric excitation, since it yields non-homogeneous terms in the linearized equations of motion of a rotor, nevertheless it may be highly influential on its dynamic response.

In this study, unbalance effects in the asymptotically stable domain of a slender parametrically excited

rotor are considered, a research topic which, to the best of the authors' knowledge, in the scientific literature has not been investigated. Rotor unbalance causes an additional harmonic load acting on flexural deflection, influencing the frequency response together with the parametric excitation. Basic models of distributed-parameter slender rotors are considered, to facilitate decoupling of the equations of motion, and the analysis of steady-state responses, including both cases in which natural frequencies are independent of, and dependent on, angular speed (i.e., on the external excitation frequency), the latter due to gyroscopic effect.

The simplest model considered, able to study the effects of angular speed independently of variations of the natural frequencies, is a homogeneous Euler–Bernoulli beam with circular section, rotating at constant angular speed about its longitudinal axis on isotropic supports, affected by unbalance and loaded by an axial end thrust, assumed to have a harmonic time-dependent component. It is also assumed that the lateral displacement of the beam is so small that axial motions are negligible, meaning that the axial excitation frequency does not induce axial resonance. Shear and gyroscopic effects are studied separately, to facilitate decoupling of the equations of motion of the parametrically excited rotor: first, by adding the shear deformation term in the Euler–Bernoulli model (Euler–Bernoulli model plus shear) [32]; second, by adding the rotary inertia and the gyroscopic effect of the beam to the translational inertia (Rayleigh model).

The steady-state response is analytically investigated in the frequency domain after decoupling the linear equations of motion, in exact (whenever possible) and approximate forms (to facilitate the analysis, in the presence of both damping and gyroscopic terms), yielding scalar non-homogeneous Mathieu-Hill equations, either in real or complex coordinates, cast in full dimensionless form to generalize the results.

The analysis is aimed at showing how the presence of non-homogeneous terms due to unbalance, together with parametric excitation, can affect the frequency response of the rotor, on combination external resonances, and on the flexural critical speeds.

Section 2 presents a description of the above-mentioned basic rotor models, Sect. 3 recalls the mathematical expression of the steady-state response, of general validity, Sect. 4 presents a series of general remarks about the steady-state response, Sect. 5 shows the results of the frequency response analysis and their discussion, also compared with some partial results found in the literature.

2 Model description and equations of motion

Three basic distributed-parameter models of a spinning beam are considered: the Euler–Bernoulli model (Sect. 2.1), the Euler–Bernoulli model plus shear (Sect. 2.2), and the Rayleigh model, undamped (Sect. 2.3) and damped (Sect. 2.4). The equations of motion are decoupled either in exact or approximate forms, working in both real and complex coordinates, leading in all cases to single-degree-of-freedom non-homogeneous Mathieu-Hill equations to facilitate the analysis of steady-state responses, cast in full dimensionless form to generalize the results.

2.1 Euler–Bernoulli model

The simplest rotor model here considered consists of a homogeneous Euler–Bernoulli straight beam with circular section, rotating at constant angular speed about its longitudinal axis on isotropic supports at both ends [21]. It is affected by unbalance and loaded by an axial end thrust, time-dependent and harmonic, i.e. $N(t) = \Delta N \cos(\omega_N t)$, positive if tensile. A stationary component in N is not considered, without loss of generality in the present analysis. The equations of motion can then be written in a non-rotating x, y, z Cartesian coordinate system, in which x coincides with the rotation axis of the shaft, as shown in Fig. 1,

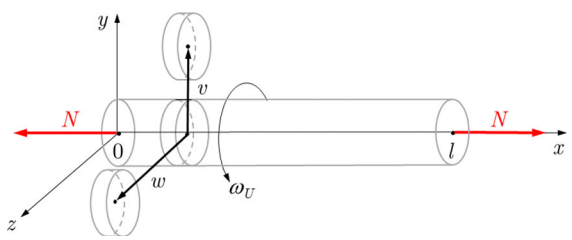

Fig. 1 Schematic representation of the rotor under analysis

adopting a notation in which dots indicate differentiation with respect to time t, and roman numbers indicate differentiation with respect to the spatial variable x (in particular, the superscript 'II' will denote the second partial derivative with respect to x, and the superscript 'IV' will denote the fourth partial derivative with respect to x):

$$\begin{cases} \rho A\,\ddot{v} + EIv^{IV} - \Delta N\cos(\omega_N t)v^{II} = \rho A\,\omega_U^2 f_v(x,t) \\ \rho A\,\ddot{w} + EIw^{IV} - \Delta N\cos(\omega_N t)w^{II} = \rho A\,\omega_U^2 f_w(x,t) \end{cases}$$
$$\begin{cases} f_v(x,t) = e_y(x)\cos(\omega_U t+\varphi) - e_z(x)\sin(\omega_U t+\varphi) \\ f_w(x,t) = e_y(x)\sin(\omega_U t+\varphi) + e_z(x)\cos(\omega_U t+\varphi) \end{cases} \tag{1}$$

where v and w are the displacements in the y and z directions, respectively, ρ represents the density of the shaft, A its cross-section area, I the planar moment of inertia of the cross-section of the shaft, E the Young's modulus, ω_U the angular speed, ΔN the amplitude of the parametric excitation, ω_N its angular frequency, $e_y(x)$ and $e_z(x)$ are the mass eccentricity distributions in the y and z directions, while φ is the phase-lag between parametric and external excitations.

Separating the variables, assuming boundary conditions making decoupling possible using Euler–Bernoulli eigenfunctions (as simply supported ends), and introducing an external damping distribution (making decoupling possible as well, as discussed in [35]), the problem can be reduced to the study of the following scalar equation:

$$\ddot{\eta}_n + 2\zeta_n\omega_n\dot{\eta}_n + \left[\omega_n^2 + a_n\cos(\omega_N t)\right]\eta_n = e_n\omega_U^2\cos(\omega_U t+\psi_n) \tag{2}$$

where η_n is the n^{th} modal coordinate, ω_n is the n^{th} natural angular frequency, ζ_n is the n^{th} modal damping ratio, a_n is the n^{th} modal parametric excitation amplitude, e_n is the n^{th} modal unbalance amplitude and ψ_n is the n^{th} modal phase-lag. The analysis is herein developed on basic dissipative models, as in [35]. However, it would be possible to define equivalent damping ratios [37], which may be included in Eq. (2), even for more advanced damping models.

The modal parameters in Eq. (2) can be expressed in integral form by applying a weighted residual method [38] together with exact eigenfunctions:

$$a_n = -\frac{\Delta N}{m_n}\int_0^l \phi_n^{\text{II}}(x)\phi_n(x)\,dx, \quad m_n = \rho A\int_0^l \phi_n^2(x)\,dx$$
$$e_n = \frac{\rho A}{m_n}\sqrt{\left[\int_0^l e_y(x)\phi_n(x)dx\right]^2 + \left[\int_0^l e_z(x)\phi_n(x)dx\right]^2} \tag{3}$$

where m_n is the n^{th} modal mass and ϕ_n is the n^{th} eigenfunction. In the case of simply supported ends, the well-known expressions of the modal parameters are:

$$m_n = \rho A, \quad k_n = EI\left(\frac{n\pi}{l}\right)^4$$
$$\omega_n = \sqrt{\frac{EI}{\rho A}}\left(\frac{n\pi}{l}\right)^2, \quad a_n = \frac{\Delta N}{\rho A}\left(\frac{n\pi}{l}\right)^2 \tag{4}$$

where k_n is the n^{th} modal stiffness. Defining a dimensionless time τ, two dimensionless frequencies, a normalized amplitude of the parametric excitation and a normalized modal coordinate as:

$$\tau = \omega_n t, \quad \omega = \frac{\omega_U}{\omega_n}, \quad \Omega = \frac{\omega_N}{\omega_n}, \quad \alpha_n = \frac{a_n}{\omega_n^2}, \quad \eta_{0n} = \frac{\eta_n}{e_n} \tag{5}$$

yields the following dimensionless form of the damped Mathieu-Hill equation with external harmonic forcing term:

$$\frac{d^2\eta_{0n}}{d\tau^2} + 2\zeta_n\frac{d\eta_{0n}}{d\tau} + [1+\alpha_n\cos(\Omega\tau)]\eta_{0n} = \omega^2\cos(\omega\tau+\psi_n) \tag{6}$$

Equation (6) allows the analysis of the modal frequency response in terms of five dimensionless governing parameters: normalized frequency of the unbalance excitation ω, normalized frequency and amplitude of the parametric excitation Ω, α_n, damping factor ζ_n, and phase-lag ψ_n.

2.2 Euler–Bernoulli model plus shear effect

The shear effect is added to the model according to [32], using a standard complex notation:

$$u = v + iw \tag{7}$$

Consequently, the equilibrium equations Eq. (1) can be rewritten in complex form as:

$$\rho A\ \ddot{u} + EI\, u^{\mathrm{IV}} - \Delta N \cos(\omega_N t)\, u^{\mathrm{II}} = \rho A\, \omega_U^2 [f_v(x,t) + i f_w(x,t)] = F \tag{8}$$

A shear term is added to Eq. (8), yielding:

$$\rho A\ \ddot{u} + EI\, u^{\mathrm{IV}} - \chi \rho I \frac{E}{G} \ddot{u}^{\mathrm{II}} - \Delta N \cos(\omega_N t)\, u^{\mathrm{II}} = F \tag{9}$$

where G is the shear modulus and χ is the shear factor, representing the Euler–Bernoulli model plus shear, which does not include any effect related to the rotation of the shaft in the homogeneous part of the equilibrium equation.

Assuming boundary conditions making decoupling possible using Euler–Bernoulli eigenfunctions (as simply supported ends), Eq. (9) can be written in the form of Eq. (2) introducing also in this case a damping term, with same modal stiffness, but with different modal mass, which in the case of simply supported ends is given by:

$$m_n = \rho A + \chi \rho I \frac{E}{G} \left(\frac{n\pi}{l}\right)^2 \tag{10}$$

According to Eq. (10), due to shear effect, the modal mass m_n is increased (with modal stiffness k_n unchanged), reducing the natural angular frequency ω_n, the modal damping ratio ζ_n, the modal parametric excitation amplitude a_n, and the modal unbalance amplitude e_n.

It is important to note that also in this case the descending dimensionless Mathieu equation can be written in the same form as Eq. (6). Therefore, even though the modal mass m_n changes, and consequently also the modal parameters (ω_n, ζ_n, a_n, e_n), the analysis and results about the stable steady-state response of the rotor given in dimensionless form are valid for both the Euler–Bernoulli model and the Euler–Bernoulli model plus shear, as it will be discussed and clarified in Sect. 5.1.

2.3 Rayleigh model (gyroscopic effect), undamped

Following the same approach as in Sect. 2.2, the equilibrium equations Eq. (1) is rewritten using the complex notation. Then the rotary inertia of the cross-section and the gyroscopic effect can be added to the model, yielding:

$$\rho A\ \ddot{u} - I_m \ddot{u}^{\mathrm{II}} + i J_m \omega_U \dot{u}^{\mathrm{II}} + EI\, u^{\mathrm{IV}} - \Delta N \cos(\omega_N t)\, u^{\mathrm{II}} = F \tag{11}$$

where I_m is the diametral (cross-section) mass moment of inertia per unit length and J_m is the polar (cross-section) mass moment of inertia per unit length of the shaft (due to symmetry, $J_m = 2I_m$). Equation (11) represents the Rayleigh model for flexural oscillations of a spinning shaft, including a parametric excitation term [32].

Assuming boundary conditions making decoupling possible using Euler–Bernoulli eigenfunctions (as simply supported ends), Eq. (11) yields the following modal equilibrium equation in complex coordinates:

$$\ddot{q}_n - i(\gamma_n \omega_U)\, \dot{q}_n + \left[\omega_n^2 + a_n \cos(\omega_N t)\right] q_n = \frac{f_n}{m_n} = e_n \omega_U^2\, e^{i(\omega_U t + \psi_n)} \tag{12}$$

where q_n is a complex modal coordinate, γ_n is the modal parameter related to the gyroscopic term, and f_n is the modal component of the external load. In the case of simply supported ends the modal parameters in Eq. (12) take the form:

$$\begin{aligned} m_n &= \rho A + I_m \left(\frac{n\pi}{l}\right)^2, \quad k_n = EI \left(\frac{n\pi}{l}\right)^4 \\ \gamma_n &= \frac{J_m}{m_n} \left(\frac{n\pi}{l}\right)^2, \quad a_n = \frac{\Delta N}{m_n} \left(\frac{n\pi}{l}\right)^2 \end{aligned} \tag{13}$$

Note that $\gamma_n < 2$, since $J_m = 2I_m$ (γ_n is monotonic increasing with n, tending to 2 as n tends to infinity).

The characteristic equation descending from Eq. (12), setting $\Delta N = 0$ (no parametric excitation), yields a pair of complex, non-conjugate (imaginary) roots:

$$s_{1,2} = i \left[\frac{1}{2} \gamma_n \omega_U \pm \sqrt{\omega_n^2 + \frac{1}{4} (\gamma_n \omega_U)^2} \right] \tag{14}$$

Another pair of complex, non-conjugate (imaginary) roots descend from the adjoint problem (imposing negative angular speed ω_U [39–41]), yielding the two pair of complex conjugate (imaginary) forward (f) and backward (b) roots (and related natural angular frequencies):

$$s_{1,2}^{(f)} = \pm i\left(\omega_{nm} + \frac{1}{2}\gamma_n\omega_U\right),$$
$$s_{1,2}^{(b)} = \pm i\left(\omega_{nm} - \frac{1}{2}\gamma_n\omega_U\right) \tag{15}$$

where ω_{nm} represents the mean value between the forward and backward natural angular frequencies:

$$\omega_{nm} = \frac{\left|s_1^{(f)} + s_1^{(b)}\right|}{2} = \sqrt{\omega_n^2 + \frac{1}{4}\left(\gamma_n\omega_U\right)^2} \tag{16}$$

The same result could also be obtained working with real coordinates, as shown in the Appendix.

Note that the forward and backward natural angular frequencies, as their mean value, depend on the angular speed, and therefore on the excitation frequency of the external load (unbalance), making the analysis of the system's response more difficult than in the previous cases.

Note also that a forward (modal) critical speed occurs only if $\gamma_n < 1$, since if $\gamma_n \to 1$, the forward critical speed tends to infinity. Hence $\gamma_n = 1$ is a discriminant value, as it will be clarified with more details in Sect. 5.2.

To facilitate analytical developments, it is now convenient to reduce Eq. (12) to the simpler form of the undamped Eq. (2). To this purpose, the following coordinate transformation is adopted [42]:

$$q_n = g_n e^{+\frac{1}{2}i\gamma_n\omega_U t} \tag{17}$$

and introduced into the model with parametric excitation ($\Delta N > 0$), Eq. (12), yielding the modal equilibrium equation in the form:

$$\ddot{g}_n + \left[\omega_{nm}^2 + a_n\cos(\omega_N t)\right] g_n = \frac{f_n}{m_n} e^{-\frac{1}{2}i\gamma_n\omega_U t} \tag{18}$$

Dimensionless parameters are defined as those in Eq. (5), with the only difference that ω_n is now replaced by ω_{nm}:

$$\hat{\tau} = \omega_{nm}\, t, \quad \hat{\omega} = \frac{\omega_U}{\omega_{nm}}, \quad \hat{\Omega} = \frac{\omega_N}{\omega_{nm}}, \quad \hat{\alpha}_n = \frac{a_n}{\omega_{nm}^2}, \quad \hat{\eta}_{0n} = \frac{g_n}{e_n} \tag{19}$$

Note that ω_{nm} depends on the angular speed ω_U through Eq. (16), and so also the time scaling. Whilst the angular speed ω_U is a theoretically unbounded parameter, as well as its dimensionless representation ω in Eq. (5), this is not true for $\hat{\omega}$ in Eq. (19). In fact, as $\omega_U \to \infty$, then $\hat{\omega} \to 2/\gamma_n$, hence $\hat{\omega} < 2/\gamma_n$ is bounded.

Equation (18) can then be rewritten in the following full dimensionless form:

$$\frac{d^2\hat{\eta}_{0n}}{d\tau^2} + \left[1 + \hat{\alpha}_n\cos(\hat{\Omega}\hat{\tau})\right]\hat{\eta}_{0n} = \hat{\omega}^2 e^{i\,(\hat{\omega}_f\hat{\tau}+\psi_n)}$$
$$\hat{\omega}_f = \left(1 - \frac{1}{2}\gamma_n\right)\hat{\omega} \tag{20}$$

where the normalized modal coordinate given in Eq. (19) is now complex, as the non-homogeneous term. Equation (20) is a dimensionless form of the undamped Mathieu equation with an external harmonic forcing term. It reduces to the undamped version of Eq. (6) by setting $\gamma_n = 0$ (no gyroscopic effect, Euler–Bernoulli model).

Comparing Eq. (6) without damping with Eq. (20), apart from the obvious difference given by adopting different symbols to distinguish the normalization in Eq. (19) from that in Eq. (5), the most important difference is due to the gyroscopic term, producing a frequency shift in the imaginary exponent on the right-hand side of Eq. (20). This means that the forward resonance of the non-parametrically excited system ($\Delta N = 0$) does not occur at ω_{nm}, as it would happen by setting $\gamma_n = 0$ in Eq. (20). Actually, it occurs at a larger value, given by the forward natural angular frequency, Eq. (15):

$$\omega_{nf} = \omega_{nm} + \frac{1}{2}\gamma_n\omega_U \tag{21}$$

which is a critical speed of the rotor. This resonance occurs at the forward natural angular frequency since the forcing term, due to unbalance, acts at a frequency given by the (forward) angular speed ω_U.

2.4 Rayleigh model (gyroscopic effect), damped

The modal equilibrium equation in complex coordinates Eq. (12) is rewritten including a modal damping term, considering the realistic presence of a certain amount of external (non-rotating) damping [35]:

$$\ddot{q}_n + (2\zeta_n\omega_n - i\gamma_n\omega_U)\dot{q}_n + \left[\omega_n^2 + a_n\cos(\omega_N t)\right]q_n = e_n\omega_U^2 e^{i(\omega_U t+\psi_n)} \tag{22}$$

where ζ_n is the modal damping factor.

Note that the characteristic equation descending from Eq. (22), setting $\Delta N = 0$ (no parametric excitation), reads:

$$s^2 + (2\zeta_n\omega_n - i\,\gamma_n\omega_U)\,s + \omega_n^2 = 0 \tag{23}$$

yielding two complex non-conjugate roots:

$$s_{1,2} = -\zeta_n\omega_n + i\,\frac{1}{2}\gamma_n\omega_U \pm i\sqrt{\omega_n^2(1-\zeta_n^2) + \frac{1}{4}(\gamma_n\omega_U)^2 + i\,\zeta_n\gamma_n\omega_n\omega_U} \tag{24}$$

Under the realistic assumption of small damping amounts, and hence setting $\zeta_n^2 \cong 0$, the two complex non-conjugate roots in Eq. (24) can be rewritten as:

$$s_{1,2} \cong -\zeta_n\omega_n\left(1 \pm \frac{1}{2}\frac{\gamma_n\omega_U}{\omega_{nm}}\right) + i\,\omega_{nm}\left(\pm 1 + \frac{1}{2}\frac{\gamma_n\omega_U}{\omega_{nm}}\right)$$
$$\gamma_n\hat{\omega} = \frac{\gamma_n\omega_U}{\omega_{nm}} = \frac{\gamma_n\omega}{\sqrt{1+\frac{1}{4}(\gamma_n\omega)^2}} < 2 \quad \Rightarrow \quad \mathrm{Re}\left[s_{1,2}\right] < 0 \tag{25}$$

which means that a separation occurs between forward and backward eigenvalues also in their real parts, and that the backward eigenvalue (minus signs) has a smaller (in modulus) real part, tending to 0 as the angular speed ω_U tends to infinity. Note that the ratio $\gamma_n\omega_U$ / ω_{nm} in Eq. (25) is monotonic increasing with the angular speed, yielding a negative real part of s_2 even at extremely high values of angular speed. If the ratio $\gamma_n\omega_U$ / ω_{nm} is sufficiently low, i.e. when the factor $\gamma_n\omega$ is sufficiently small, and considering low values for the modal damping factor ζ_n, then a further simplification is possible in the expression of the two complex non-conjugate roots in Eq. (24):

$$s_{1,2} \cong -\zeta_n\omega_n + i\left(\frac{1}{2}\gamma_n\omega_U \pm \omega_{nm}\right) \tag{26}$$

The roots in Eq. (26) have the same real part, and imaginary parts which are the same as in Eq. (14). This simplifying assumption underestimates external damping in the forward eigenvalue; hence it is conservative for amplitude estimation of forward resonance peaks.

Considering the same simplifying assumptions leading to Eq. (26), and applying the coordinate transformation Eq. (17) to Eq. (22), gives the modal equilibrium equation in the form:

$$\ddot{g}_n + 2\zeta_n\omega_n\dot{g}_n + \left[\omega_{nm}^2 + a_n\cos(\omega_N t)\right]g_n = \frac{f_n}{m_n}e^{-\frac{1}{2}i\gamma_n\omega_U t} \tag{27}$$

which is the same as Eq. (18), plus a modal damping term. Recalling Eqs. (18) and (19), Eq. (27) can be finally rewritten in dimensionless form, as Eq. (20):

$$\begin{cases} \dfrac{d^2\hat{\eta}_{0n}}{d\tau^2} + 2\hat{\zeta}_n\dfrac{d\hat{\eta}_{0n}}{d\tau} + \left[1 + \hat{\alpha}_n\cos(\hat{\Omega}\hat{\tau})\right]\hat{\eta}_{0n} = \hat{\omega}^2 e^{i\left[\hat{\omega}_f\hat{\tau}+\psi_n\right]}, \\ \hat{\omega}_f = \left(1 - \dfrac{1}{2}\gamma_n\right)\hat{\omega} \end{cases} \tag{28}$$

where an equivalent damping ratio is defined:

$$\hat{\zeta}_n = \frac{\zeta_n}{\sqrt{1+\frac{1}{4}(\gamma_n\omega)^2}} < \zeta_n \tag{29}$$

which depends on the gyroscopic parameter γ_n. The gyroscopic effect tends to reduce the damping ratio in Eq. (29), however, under the assumption of a small factor $\gamma_n\omega$, this correction may be negligible.

Equation (28), compared with Eq. (22), has the simpler form of Eq. (6). Therefore, as Eq. (20), its use is convenient to facilitate analytical developments.

However, for comparison with respect to the case with no gyroscopic effect in terms of direct numerical computation of the response, it is more convenient casting Eq. (22) in dimensionless form by means of the parameters defined in Eq. (5), which avoids the difficulty given by the normalization in Eq. (19), involving a parameter (ω_{nm}) dependent on the angular speed:

$$\begin{cases} \dfrac{d^2q_{0n}}{d\tau^2} + (2\zeta_n - i\gamma_n\omega)\dfrac{dq_{0n}}{d\tau} + [1 + \alpha_n\cos(\Omega\tau)]q_{0n} = \omega^2 e^{i(\omega\tau+\psi_n)} \\ q_{0n} = \dfrac{q_n}{e_n} \end{cases} \tag{30}$$

which is a differential equation with a complex coefficient, where q_{n0} is a dimensionless complex modal coordinate.

In conclusion of this Section, the model described by Eq. (6) can be used for studying the steady-state response of the unbalanced and parametrically excited stable rotor without shear and gyroscopic effects, as well as in the case of the Euler Bernoulli model plus shear. On the other hand, Eq. (6) should be replaced either by Eq. (20), undamped case, or by Eqs. (28) and

(30), damped case, for studying the effects of gyroscopic actions on the steady-state response of the rotor.

Equations (6), (20), (28) and (30) are modal equilibrium equations in full dimensionless form. Therefore, different boundary conditions would affect the values of the modal parameters given in Eqs. (4) and (10), but not the steady-state solutions of the above-mentioned modal equilibrium equations, in terms of dimensionless parameters. This is true if the equations of motion can be decoupled into modal equilibrium equations (as for the models considered in the present study), for which the knowledge of the eigenfunctions (either in exact or approximate form) is necessary. Reference [41] provides a complete list of standard boundary conditions for a spinning beam (including as particular cases all the models adopted in the present study), with related eigenfunctions.

3 Steady-state response

The theory of non-homogeneous Mathieu-Hill equations [3] is recalled for writing the expression of the steady-state solution of Eqs. (6), (20) and (28).

Descending from an application of the Floquet-Fourier-Hill method [43], the solutions of the homogeneous equations associated to Eqs. (6), (20) and (28) can be expressed as the product of an exponential function (with an unknown exponential coefficient, say Λ) by a periodic function represented by a truncated Fourier series of (dimensionless) period T:

$$\mathrm{T} = 2\pi/\Omega \tag{31}$$

This yields an algebraic quadratic eigenproblem, where the eigenvalues Λ are called characteristic exponents [4], which can be normalized according to:

$$\lambda = \Lambda/\Omega \tag{32}$$

and linked to the Floquet multipliers μ [4] by the following exponential relation:

$$\mu = e^{\left(\Lambda \pm i\frac{2\pi}{\mathrm{T}}\right)\mathrm{T}} = e^{\Lambda\,\mathrm{T}} = e^{\lambda\,\Omega\,\mathrm{T}} = e^{2\pi\lambda} = e^{2\pi(\lambda+iz)},\quad z \in \mathbb{Z} \tag{33}$$

According to [3], the steady-state solution of the non-homogeneous equation, Eq. (6), in its asymptotically stable domain (say η_{0nss}), can be written in the form:

$$\eta_{0nss}(\tau) = \mathrm{Re}\left[C_{hkj}\left(\frac{\omega^2 e^{i(\omega+q\Omega)\tau}}{i(\omega+k\Omega)-\Lambda_j}\right)\right] \tag{34}$$
$$h,k \in \mathbb{Z},\quad q = h+k,\quad j = 1,\,2$$

where C_{hkj} implicitly denotes a triple sum (with indexes h, k, j), while the eigenvalues Λ are linked to the normalized characteristic exponents λ and to the Floquet multipliers μ through Eqs. (32) and (33).

Therefore, the steady-state modal response is a linear combination of terms, each of them given by the expression in round brackets reported in Eq. (34), multiplied by a complex-amplitude coefficient, including a factor due to the phase-lag ψ_n (a frequency independent, complex exponential factor with modulus equal to unity). In the case of the model described by Eq. (6), each coefficient is a function of four governing parameters: normalized frequency and normalized amplitude of the parametric excitation (Ω, α_n), damping factor (ζ_n), and phase-lag (ψ_n). It can be shown that in this case Eq. (34) can be rewritten in the following simpler form:

$$\eta_{0nss}(\tau) = \sum_{q=-\infty}^{\infty} \mathrm{Re}\left[C_q e^{i\,(\omega+q\Omega)\tau}\right]$$
$$\eta_{0nss}(\tau) = \sum_{q=-\infty}^{\infty} \left\{A_q \cos[(\omega+q\Omega)\tau] + B_q \sin[(\omega+q\Omega)\tau]\right\} \tag{35}$$

where $A_q = \mathrm{Re}(C_q)$ and $B_q = -\mathrm{Im}(C_q)$ are real coefficients. As well as C_q, they also depend on the unbalance excitation (ω), other than on the other governing parameters (Ω, α_n, ζ_n, ψ_n). Note that Eq. (34) can be represented as a Fourier series only if ω and Ω are commensurate.

The steady-state solution of the non-homogeneous equation, Eq. (28), in its asymptotically stable domain, can be written in the same form of Eqs. (34) and (35), considering the different normalization given in Eq. (19), the presence of complex variables, and the role of the modal gyroscopic term γ_n, producing a shift in the normalized frequency of the external load ($\omega \rightarrow \hat{\omega}_f$).

Note that in the undamped case, in general, an additional term has to be added to the solution expressed in Eq. (34), due to the solution of the homogeneous equations [3]. Hence, the steady-state response of the non-homogeneous system, Eq. (20), can be studied in the form of Eqs. (34) and (35) as a limit case of Eq. (28), considering $\zeta_n \rightarrow 0$.

Note also that the series in Eq. (34), as originally derived in [3], is valid for multiple-degree-freedom systems, it considers the possibility of having a periodic parametric excitation (not necessarily given by a single harmonic term), and it considers a single harmonic term in the external excitation, however showing that in the latter case the superposition principle holds true.

When considering a parametric excitation term expressed by a Fourier series, it is known that higher-order harmonics can change significantly the results in terms of stability analysis [9, 44, 45], therefore it is expected that they also affect the system's frequency response in stable conditions. In the present study, however, the analysis is focused on a single harmonic term in the parametric excitation.

4 General remarks on the steady-state response

In this Section, the notation valid in the case with no gyroscopic effect, Eq. (5), is adopted. However, most results are valid also in the case with gyroscopic effect, except for a few of them, explicitly highlighted, needing further developments and comments, for which the reader is referred to Sect. 5.3.

The steady-state response, Eq. (34) can be studied according to the following 10 remarks:

1. *Periodicity of the solution*. The steady-state response of the asymptotically stable system given in Eq. (34) is periodic only if ω and Ω are commensurate, i.e. only if the ratio:

$$\frac{\omega}{\Omega} = \frac{\omega_U}{\omega_N} = R, \quad R \in \mathbb{Q} \tag{36}$$

   is a rational number, as it descends clearly from Eq. (35). Note that the periodicity of the solution does not depend on the natural angular frequency.
2. *Maximum amplitude of the steady-state response*. If, for a given set of values of the governing parameters (in the presence of damping), the solution is periodic, then it is always possible to calculate its maximum amplitude (the accuracy depending on truncation errors in the Fourier series).
3. *Diagram of maximum amplitudes of the steady-state response*. Since each given ratio ω / Ω can always be approximated by a rational number R, the maximum amplitude defined in point 2 can be represented as a function of ω / $\Omega = R$ in a diagram, as displayed below in Figs. 2, 3, 4, 5, 6, 7, 8, 9, and 11 (maximum amplitudes A_{max} of the steady-state response, normalized to get unitary amplitude in the case of $a_n = 0 \Rightarrow \alpha_n = 0$, i.e. in the case with no parametric excitation).
4. *Differences between the diagram of maximum amplitudes, and representation of the modulus of frequency response functions of linear-time-invariant systems*. This becomes evident considering that at different values ω / $\Omega = R$, the steady-state responses are characterized by different periods (tending to infinity whenever R approaches an irrational number), and by different harmonic spectra, affecting the waveforms (in general not given by a simple harmonic term). Therefore, additional information for a better characterization of the steady-state responses is provided by combining the diagram of maximum amplitudes of periodic waveforms, with the diagram of their RMS values, as displayed in Figs. 7, 8 and 9.
5. *Resonances in the case* $\zeta_n \to 0$. For any fixed value of Ω, the values of ω causing resonances can be easily identified at least when ζ_n tends to zero, i.e., when the real part of Λ_j in Eq. (34) tends to zero (practically, considering a sufficiently low modal damping amount), yielding the following sequence:

$$\begin{aligned} &\omega = \Omega\,(\pm\lambda_{im} + k), \quad k = 0, 1, 2, ..., \\ &0 \le \lambda_{im} \le 0.5 \quad (\lambda_{im} = 0 \;\; \Rightarrow \;\; k \neq 0) \end{aligned} \tag{37}$$

   where λ_{im} is the minimum absolute value of Im(λ). Which can also be rewritten in terms of a sequence λ_k:

$$\begin{aligned} &\frac{\omega}{\Omega} = (\pm\lambda_{im} + k) \;\; = \lambda_k \\ &= (\lambda_{im},\; 1 - \lambda_{im},\; 1 + \lambda_{im},\; 2 - \lambda_{im},\; 2 + \lambda_{im} \ldots) \end{aligned} \tag{38}$$

   Hence, resonances occur depending on the values taken by the characteristic exponents. For any fixed value of λ_{im}, Eq. (38) proves that in the diagram of maximum amplitudes as a function of ω / Ω, the position of resonances

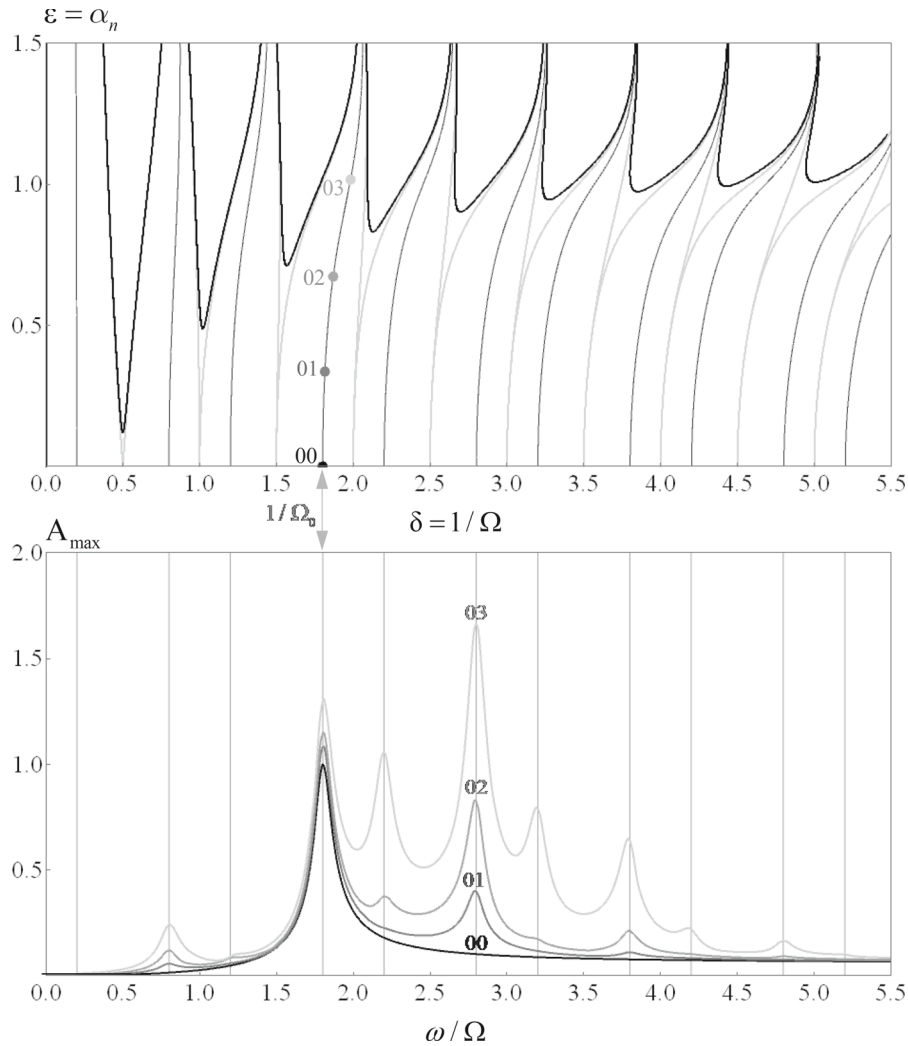

Fig. 2 Ince-Strutt diagram drawn at $\zeta_n = 0.03$, with a sequence of iso-λ_{im} curves (top), and maximum amplitude diagram drawn at different values of α_n (bottom)

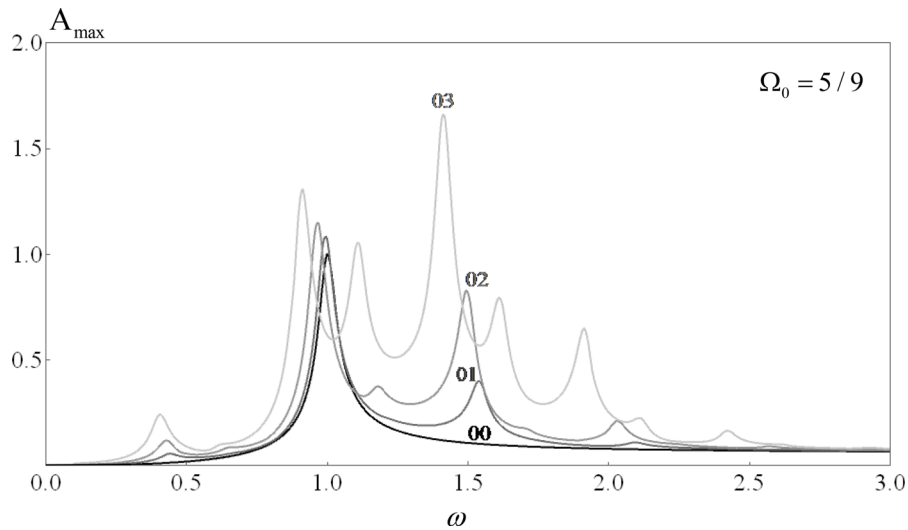

Fig. 3 Maximum amplitude diagram, same parameters as in Fig. 2, but drawn as a function of ω

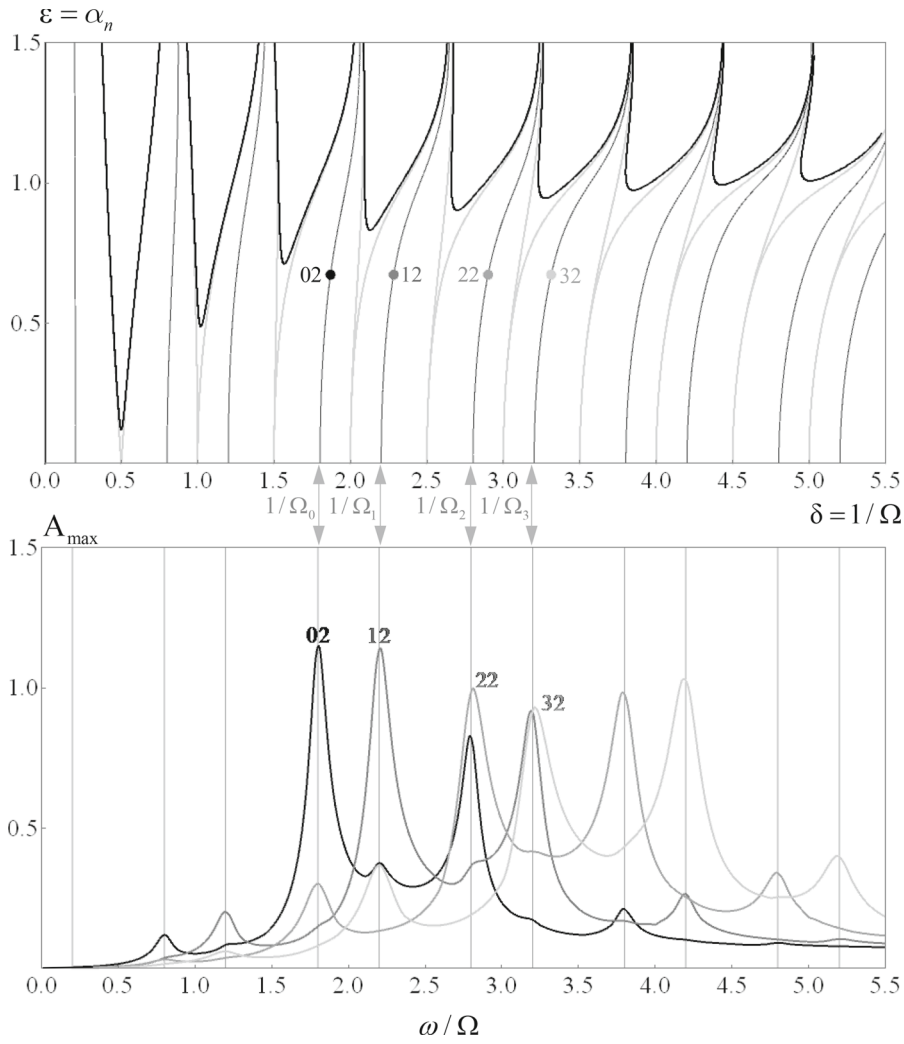

Fig. 4 Ince-Strutt diagram drawn at $\zeta_n = 0.03$, with a sequence of iso-λ_{im} curves (top), and maximum amplitude diagram drawn at different values of Ω_j (bottom)

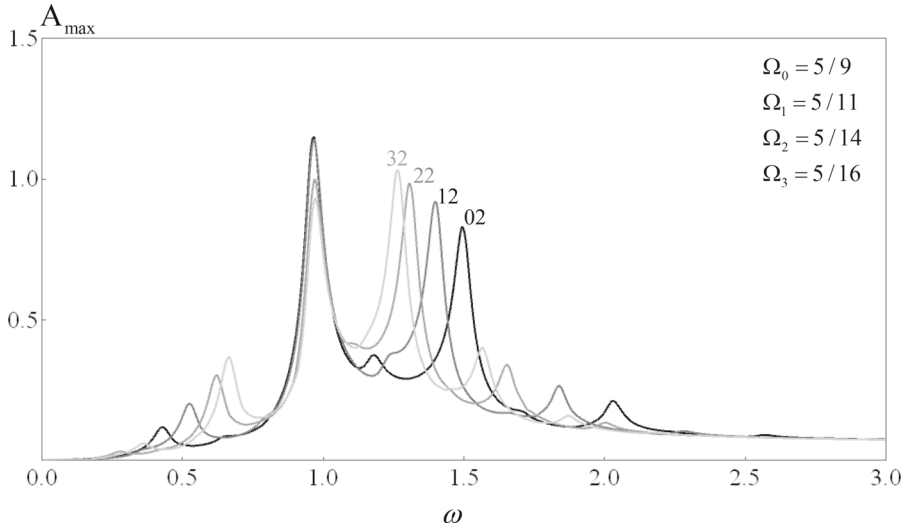

Fig. 5 Maximum amplitude diagram, same parameters as in Fig. 4, but drawn as a function of ω

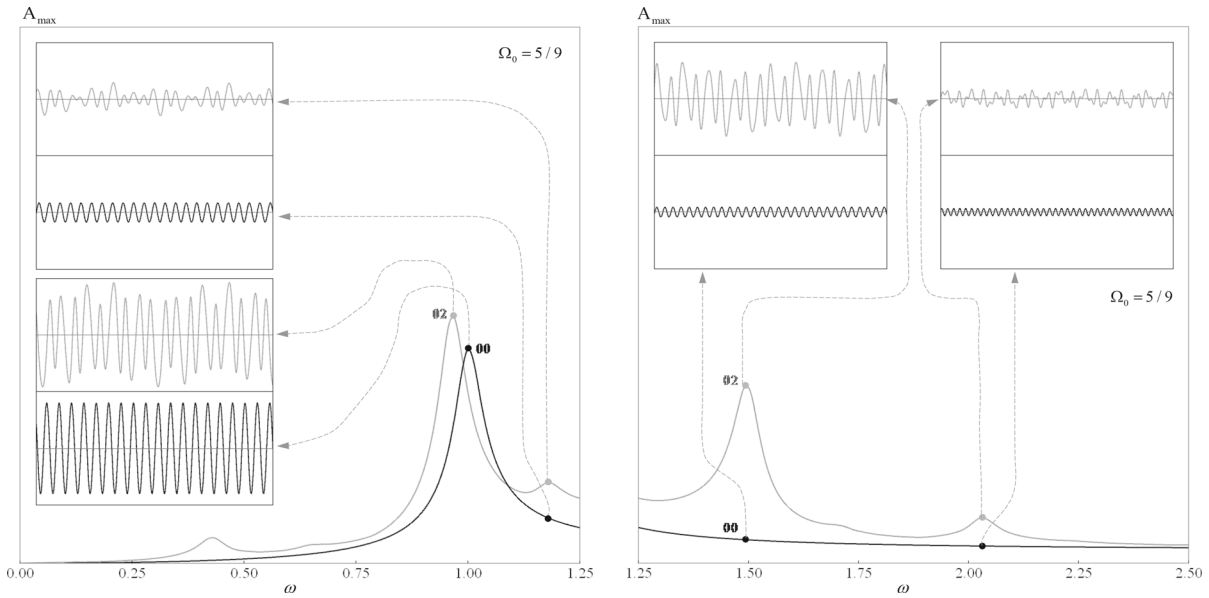

Fig. 6 Maximum amplitude diagram, as in Fig. 2, and steady-state response signals at resonances (η_{0nss} functions of τ)

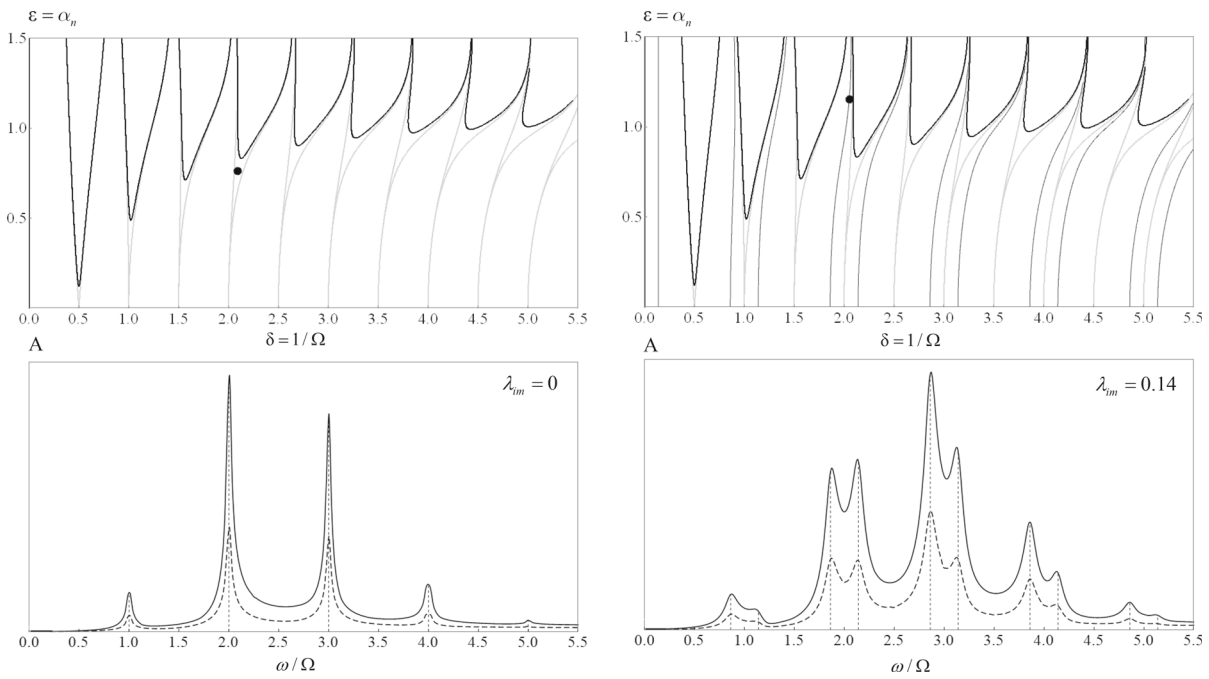

Fig. 7 Ince-Strutt diagrams (top), maximum amplitude (solid line) and RMS value (dashed line) diagrams (bottom), drawn at different operating conditions, identified by black dots ($\lambda_{im} = 0$ and $\lambda_{im} = 0.14$)

when $\zeta_n \to 0$, given by λ_k, remains unchanged. Also, if a resonance occurs at an irrational value of ω / Ω, then the undamped response will evolve with oscillations increasing in amplitude, with no exact pseudo-period. Therefore, in the presence of damping, the value taken by λ_{im} can generate resonances with non-periodic responses. In some cases, these responses may be quasi-periodic.

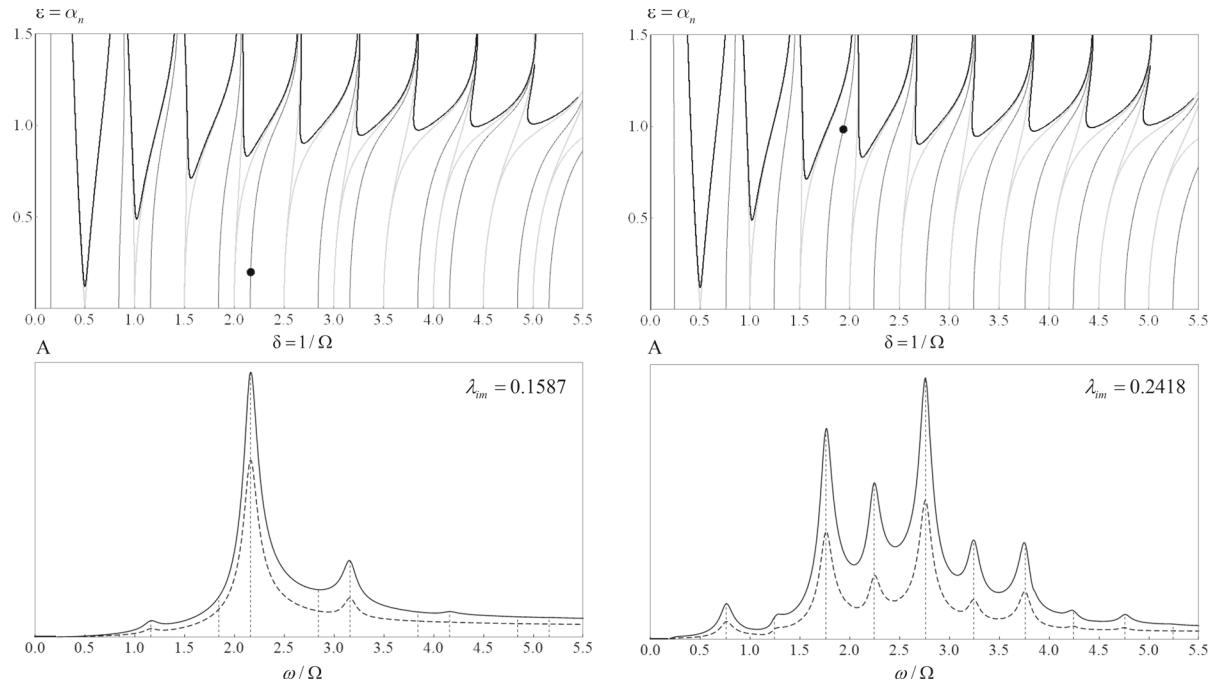

Fig. 8 Ince-Strutt diagrams (top), maximum amplitude (solid line) and RMS value (dashed line) diagrams (bottom), drawn at different operating conditions, identified by black dots (λ_{im} = 0.1587 and λ_{im} = 0.2418)

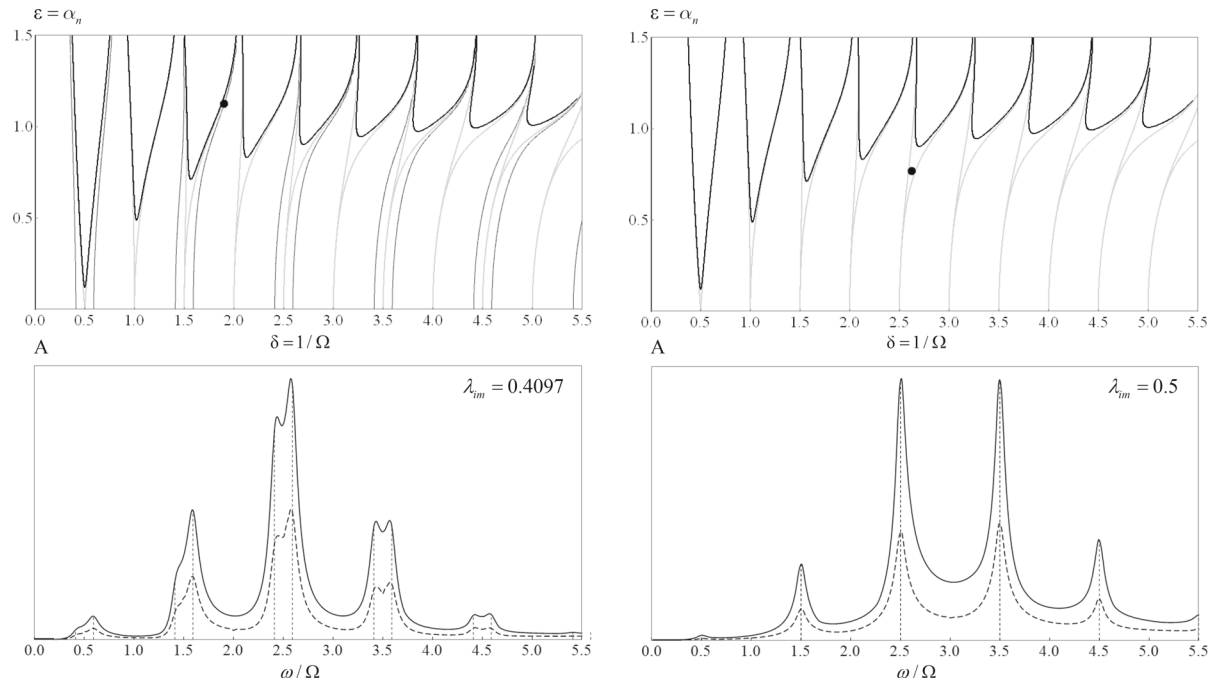

Fig. 9 Ince-Strutt diagrams (top), maximum amplitude (solid line) and RMS value (dashed line) diagrams (bottom), drawn at different operating conditions, identified by black dots (λ_{im} = 0.4097 and λ_{im} = 0.5)

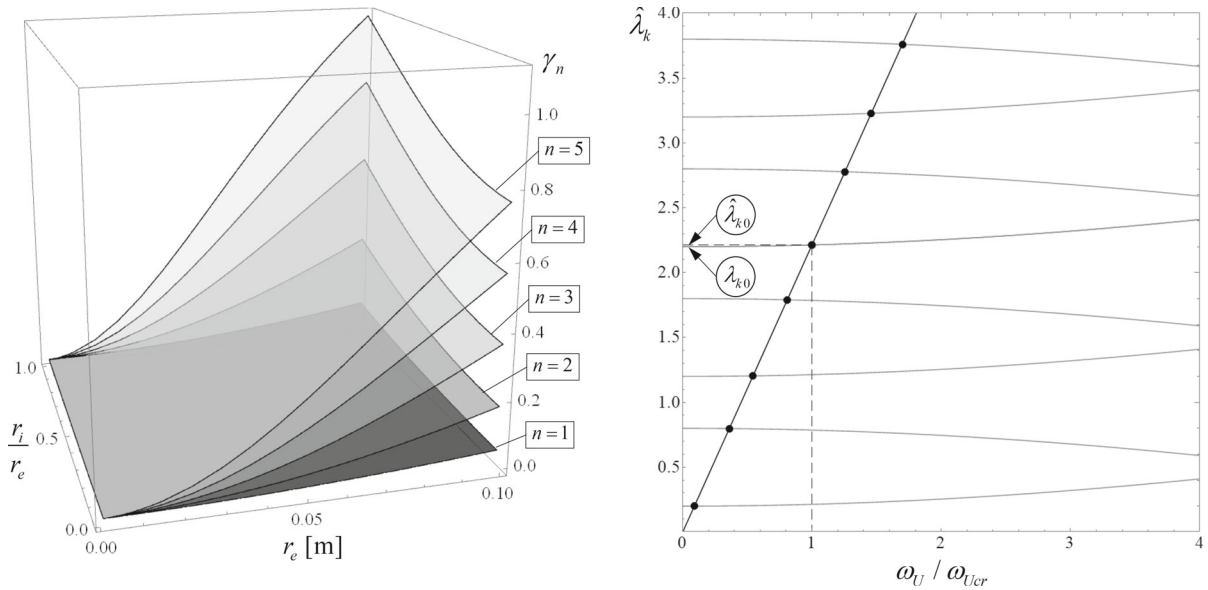

Fig. 10 Values of γ_n for modes 1–5 of an iron shaft with length $l = 1$ m and hollow circular section (left) Sequence of resonances (dots) as $a_n \to 0$ in presence of gyroscopic effects, with $\lambda_{k0} = 11/5$ and $\gamma_n = 0.2$ (right).

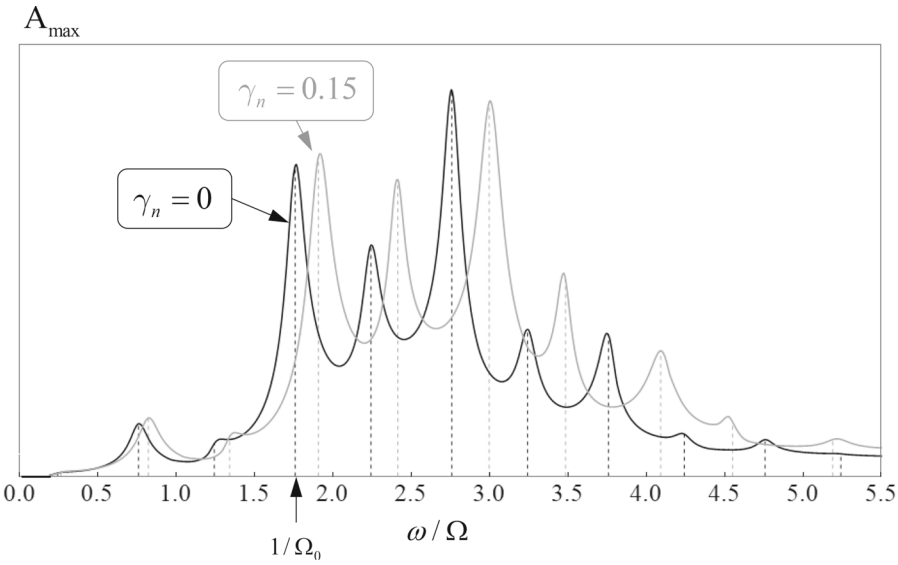

Fig. 11 Comparison of the maximum amplitude diagram already displayed in in Fig. 8, right (black curve; $\gamma_n = 0$, $\zeta_n = 0.03$, $\lambda_{im} = 0.2418$) with the diagram obtained with the same input parameters and considering in addition the gyroscopic effect (grey curve: $\gamma_n = 0.15$)

6. *Characteristic exponents and Floquet multipliers*. The role of the characteristic exponents in the generation of resonances, as described in point 5, can be extended in the presence of non-negligible damping, and better understood by recalling Eq. (33). It can be observed that in the case of a pair of complex conjugate Floquet multipliers within the unit circle in the complex plane (which occurs in the presence of damping), all the related characteristic exponents have the same (negative) real part Re(λ), and pairs of imaginary parts Im(λ) with opposite signs, which can be expressed by the sum of λ_{im} plus an integer number. While in the case of a pair of real Floquet multipliers, the related characteristic exponents have distinct values for their real parts (coincident in case of collision)

and only two different values for λ_{im}, either 0 or 0.5 [4].

7. *Ince-Strutt diagram*. A comparison between the diagram of maximum amplitudes and the Ince-Strutt diagram of the Mathieu-Hill equation [13, 46] is of great advantage for a deeper understanding of the steady-state response. The Ince-Strutt diagram is a stability map of the system, as a function of frequency and amplitude of the parametric excitation. Here it is convenient to represent the Ince-Strutt diagram of the homogeneous equations associated to Eqs. (6), (20), (28), as displayed in Figs. 2 and 4 (top), as a function of two frequency and amplitude parameters (say δ and ε):

$$\delta = \frac{1}{\Omega}, \quad \varepsilon = \alpha_n \tag{39}$$

which is not the common standard representation, however it has the advantage to facilitate the comparison with the diagram of maximum amplitudes of the steady-state response. The thick black curves in Figs. 2 and 4 (top), called Arnold tongues [46], represent the stability threshold of the damped system (unstable for values of δ and ε yielding points inside the tongues). Reducing the damping amount produce an extension of the Arnold tongues towards the abscissa axis of the diagram: the thin grey curves in Figs. 2 and 4 (top) represent the instability tongues in the case of no damping (tips on the δ axis). In this analysis the stability region is considered, which in the Ince-Strutt diagram includes all points outside the Arnold tongues defined by a given value of ζ_n.

8. *Response amplitudes when* $a_n \to 0$. Recalling that on the δ axis of the Ince-Strutt diagram it is $\mathrm{Im}(\lambda) = \delta = 1/\Omega$, and that without parametric excitation ($a_n = 0$), resonance only occurs at $\omega_U = \omega_n$ (i.e. at $\omega = 1$, like in the classical Jeffcott rotor model [21]), then for any chosen value of Ω (say Ω_0) this single resonance (which in the following will be referred to as principal resonance) arises at:

$$\frac{\omega}{\Omega} = \frac{1}{\Omega_0} = \frac{\omega_n}{\omega_{N0}} = \mathrm{Im}(\lambda) = \lambda_{k0}, \qquad \lambda_{im} = \lambda_{k0} - \mathrm{int}\,(\lambda_{k0}) \tag{40}$$

which descends from Eq. (38) and allows the immediate identification of both λ_{im} and k as functions of Ω_0. In the λ_k sequence, the value λ_{k0} determines the principal resonance position on the abscissa axis of both the maximum amplitudes and Ince-Strutt diagrams (as shown in Figs. 2 and 4, top and bottom), while all the other values in the λ_k sequence identify other resonances, which in the following will be referred to as secondary resonances. To this purpose, it is convenient reading the diagram of maximum amplitudes as if $\Omega = \Omega_0$, so that the only varying parameter on the abscissa axis is ω. The variation of ω (normalized angular speed) does not influence the position of resonances (vertical grey lines in the diagrams in Figs. 2 and 4, bottom, drawn at the points identified by the sequence λ_k generated by λ_{k0}). However, this happens only if λ_{im} is independent from the angular speed ω_U, as in Figs. 2 and 4, bottom, which occurs for both the Euler–Bernoulli model and the Euler–Bernoulli model plus shear, but not for the Rayleigh model.

9. *Response amplitudes when* $a_n > 0$. The sequence λ_k generated at $a_n = 0$ based on λ_{k0}, as described in point 8, identifies the positions of all potential resonances, which begin to become effective at $a_n > 0$. In the presence of damping, however, only a limited number of them produce prominent peaks, growing with increasing values of a_n (as discussed in Sects. 5.1 and 5.2, and shown in Figs. 2 and 4, bottom). Again, it is convenient reading the diagram of maximum amplitudes as if $\Omega = \Omega_0$, so that the only varying parameter on the abscissa axis is ω, which in the case of both the Euler–Bernoulli model and the Euler–Bernoulli model plus shear does not affect the position of resonances (vertical grey lines in the diagrams in Figs. 2 and 4, bottom). It should also be noted that the position of resonances is influenced by damping ($\zeta_n = 0.03$ in all cases, Figs. 2, 3, 4, 5, 6, 7, 8 9

and 11), so that the actual resonance peaks are not exactly on the vertical grey lines, drawn in the case $\zeta_n \to 0$. Increasing a_n, while keeping constant λ_{im}, generates a sequence of curves in the Ince-Strutt diagram, a curve for each value of the sequence λ_k, which is originated by λ_{k0} as in point 8 (dark grey curves in Figs. 2 and 4, top). These form a sequence of iso-λ_{im} curves. Increasing a_n, and moving on these iso-λ_{im} curves, makes it possible to clearly see the effects of the amplitude a_n of the parametric excitation on the height of each resonance peak, occurring always at the same abscissa in the maximum amplitude diagram (Fig. 2, bottom). Note that in this study the amplitude of the frequency responses is multiplied by a factor ω^2 in all cases/Superscript> in all cases, Figs. 2, 3, 4, 5, 6, 7, 8 9, and 11, increasing the amplitude with increasing values of external excitation frequency. However, simply removing the factor ω^2 in Eq. (6) would make it possible an immediate extension of the proposed analysis to a wider class of problems.

10. *Constant ratio* ω / $\Omega = R$. Great practical relevance has the case in which the ratio between the angular speed of the rotor (ω_U) and the parametric excitation frequency (ω_N) is kept constant (i.e. when the parametric excitation frequency varies proportionally to angular speed), which also occurs when parametric excitation is caused by anisotropy in the rotating parts of a machine, as it can happen in the case of cracked rotors (for which the reader is referred to the specific literature [23, 25, 26]). The diagram of maximum amplitudes above described in point 3 in this case is not very useful, since a fixed ratio R identifies just one point on the abscissa axis, at the principal resonance. Therefore, in this case it would be more meaningful to couple the Ince-Strutt diagram to a diagram of maximum amplitudes (and/or RMS values) plotted as a function of a different abscissa: either $\delta = \omega_n$ / ω_N (same abscissa of the Ince-Strutt diagram) or ω_n / ω_U, to see the sequence of principal and secondary resonances, as it will be discussed adding all the necessary details in Sect. 5.3.

5 Results and discussion

The solution for the steady-state response recalled in Sect. 3 is applied to study in the frequency domain the models of spinning beams described in Sect. 2. All results are relative to damped models, even though for the sake of simplicity some analytical derivations are obtained from Eq. (6) and Eq. (28) letting $\zeta_n \to 0$, hence also considering Eq. (20).

Then the analysis considers two cases: no gyroscopic effect (natural frequencies and characteristic exponents independent with respect to angular speed, Euler–Bernoulli model, and Euler–Bernoulli model plus shear, Sect. 5.1); non-negligible gyroscopic effect (natural frequencies and characteristic exponents dependent on the angular speed, Rayleigh model, Sect. 5.2). Finally, Sect. 5.3 deals with the particular case in which the parametric excitation frequency varies proportionally to the angular speed according to a fixed relative ratio.

The dimensionless modal equilibrium equations and related parameter values adopted in each subsection are recalled and summarized in Table 1.

5.1 Frequency response analysis, no gyroscopic effects

Considering the remarks given in Sect. 4, the diagrams displayed in Figs. 2, 3, 4, 5, 6, 7, 8 and 9 can now be discussed in the case of the Euler Bernoulli model and the Euler Bernoulli model plus shear. Both models can be studied by means of Eq. (6). Note that the modal natural frequency ω_n and the modal eccentricity e_n simply play the role of scaling factors, while the modal phase-lag ψ_n does not affect the maximum amplitudes of the responses, since in the expression of the steady-state solution, Eq. (33), it simply produces a complex exponential factor with modulus equal to unity. Note also that the diagrams are displayed in full dimensionless form, therefore, when considering dimensional parameters, attention must be paid to the achievable limits in their respective technological ranges of variation.

Figure 2 (top) displays the Ince-Strutt diagram of Eq. (6), homogeneous part, drawn setting a modal damping ratio $\zeta_n = 0.03$ and a phase-lag $\psi_n = 0$, as functions of the frequency and amplitude parameters (δ, ε) defined in Eq. (39). In the stable region of the diagram, a sequence of iso-λ_{im} curves is also

Table 1 Dimensionless modal equilibrium equations and related parameter values

Section	Equilibrium equation and parameter values
5.1	$\frac{d^2\eta_{0n}}{d\tau^2} + 2\zeta_n \frac{d\eta_{0n}}{d\tau} + [1 + \alpha_n \cos(\Omega\tau)]\eta_{0n} = \omega^2 \cos(\omega\tau + \psi_n)$
	Modal damping ratio $\zeta_n = 0.03$
	Phase-lag $\psi_n = 0$
5.2	$\frac{d^2q_{0n}}{d\tau^2} + (2\zeta_n - i\gamma_n\omega)\frac{dq_{0n}}{d\tau} + [1 + \alpha_n \cos(\Omega\tau)]q_{0n} = \omega^2 e^{i(\omega\tau+\psi_n)}$
	Modal damping ratio $\zeta_n = 0.03$
	Modal gyroscopic factor $\gamma_n = 0.15$ and $\gamma_n = 0.20$
	Phase-lag $\psi_n = 0$
5.3	$\frac{d^2\eta_{0n}}{d\tau^2} + 2\zeta_n \frac{d\eta_{0n}}{d\tau} + [1 + \alpha_n \cos(\Omega\tau)]\eta_{0n} = \omega^2 \cos(\omega\tau + \psi_n)$
	Modal damping ratio $\zeta_n = 0.03$
	Phase-lag $\psi_n = 0$
	$\Omega/\omega = p, \quad p \in \mathbb{N}^+$

displayed, drawn at $\lambda_{im} = 0.2$ (dark grey curves). It is generated at a given value ($\Omega = \Omega_0 = 5/9$) of the parametric excitation angular frequency. Four different values of normalized parametric excitation amplitude α_n are then identified by dots (labelled 00, 01, 02, 03) on the iso-λ_{im} curve departing at $\delta = 1/\Omega_0$. Those four levels of normalized parametric excitation amplitude (including $\alpha_n = 0$, point 00) are then adopted to draw consequent maximum amplitude diagrams.

Figure 2 (bottom) shows a superposition of the maximum amplitude diagrams drawn according to the above mentioned four working points in the Ince-Strutt diagram. As already noted, increasing α_n does not change the position of the (undamped) resonances in the ω / Ω domain (represented by vertical lines). Low damping amounts (in this case $\zeta_n = 0.03$) do not produce relevant shifts. In the diagram, it is clearly visible the principal resonance (at ω / $\Omega = 5/9 = 1.8$), together with secondary resonances, their onset occurring at:

$$\omega = \Omega_0 (\pm\lambda_{im} + k) \neq 1, \quad \alpha_n = 0 \tag{41}$$

Note that all values of ω in Eq. (41) produce actual resonances, since with no damping all of them would yield vertical asymptotes in the maximum amplitude diagrams.

All resonance peaks, but the principal one, vanish as $\alpha_n \to 0$. In any case, and whatever the selected value for Ω_0, at $\alpha_n = 0$ (no parametric excitation) it is clear from the diagram that only the principal resonance survives, with $\omega = 1$ (i.e. $\omega_U = \omega_n$), like in the classical Jeffcott rotor model. The peaks of secondary resonances, at different values of ω / Ω_0, are characterized by different values of prominence (which in the diagram are normalized with respect to the prominence of the peak at $\alpha_n = 0$, curve labelled 00). The sequence of resonances is theoretically infinite, but only a limited number of them produce prominent peaks in the diagram, all confined in an interval of values ω / Ω_0 close to the principal resonance. Note the presence of a peak on the left of the principal one (at lower ω), and of several peaks on its right (one of them with very high prominence). But it is also interesting the almost complete cancellation of a resonance, very close to the principal one (at ω / $\Omega_0 = 1.2$). This indeed shows that the dependency of the prominence of resonant peaks on the parametric excitation amplitude α_n and on the modal damping ratio ζ_n is not straightforward. At sufficiently large values of ω / Ω_0 (theoretically when ω / $\Omega_0 \to \infty$), all the curves in the diagram converge to the same asymptotic value (the same given by the horizontal asymptote in the classical Jeffcott rotor model, here represented by the curve labelled by 00).

Figure 3 shows the same diagram as in Fig. 2 (bottom), but displayed as a function of ω, instead of ω / Ω_0. Here, the most interesting feature is the shift of the resonance peaks with respect to ω (i.e. with respect to the normalized angular speed). By increasing the normalized parametric excitation amplitude α_n, all the peaks move towards lower values of ω, and this is due to the inflection of the iso-λ_{im} curves in the Ince-Strutt diagram.

Of great interest for rotor dynamics is the fact that the presence of a parametric excitation can lower the critical speeds of a rotor. This can be clearly observed in Fig. 3, with both the presence of a secondary resonance peak at $\omega < 1$ (in general, the prominent secondary resonance peaks at $\omega < 1$ may be more than one), and the shift of the principal resonance peak towards lower values of angular speed ω. Even though in this specific case the prominence of the secondary resonance peak at $\omega < 1$ becomes relevant only at extremely high values of α_n, nevertheless special attention should be paid to the effects on the principal resonance peak (shift towards $\omega < 1$ and increase of prominence).

Figure 4 (top) displays the same Ince-Strutt diagram shown in Fig. 2 (top), drawn adopting the same parameter values ($\zeta_n = 0.03$, $\lambda_{im} = 0.2$), the only change regarding the choice of four different working points (labelled 02, 12, 22, 32, where 02 is the same as in Fig. 2). In this case the four working points are still identified by the same value of λ_{im}, but they are now all positioned at the same normalized parametric excitation amplitude α_n, on iso-λ_{im} curves of the same sequence. This allows to study the effect of discrete variations of Ω_j while keeping constant α_n ($\Omega = \Omega_0$, Ω_1, Ω_2, Ω_3).

Figure 5 shows the same maximum amplitude diagram as in Fig. 4 (bottom), displayed as a function of ω, instead of ω / Ω_0. Here, the principal resonance peak occurs at $\omega = 1$, independently of variations of Ω. It can be noted that reducing Ω produces both a convergence of the secondary resonance peaks towards the principal one, and an evident increase of their prominence, while, as already noted, the prominence of the principal resonance peak is lowered.

Figure 6 reproduces the same diagram as in Fig. 3 (curves 00 and 02 only), split into two parts for showing steady-state response signals at some resonance points. Even small variations in the governing parameters, can strongly affect the signals in terms of both their period, and their waveform.

This can be even better understood looking at the diagrams displayed in Figs. 7, 8, 9, showing different points on the Ince-Strutt diagrams, with respect to those selected for drawing the plots in Figs. 2, 3, 4, 5, and 6. Great spectral differences can be observed in the related maximum amplitude diagrams (solid lines), on which also the RMS values are displayed (dashed lines), putting in evidence the crest factors (the RMS values are computed on discretized time-domain responses, with equally spaced samples). The amplitudes of the frequency responses in terms of RMS values follow patterns similar to those of the maximum amplitudes. However, the scaling factor between the two amplitudes is not exactly constant with frequency. Even small changes in the characteristic exponent (λ_{im}) can produce dramatic changes in the sequence of resonant peaks, and when two adjacent peaks get closer each other, it is also possible to see a certain degree of merging, as in Fig. 9 (left).

It is important to note that the sequences given in Eqs. (37) and (38) also identify the resonances of the Euler Bernoulli model plus shear. In this case the resonances occur at different values of ω / $\Omega = \omega_U$ / ω_N, due to a different value of λ_{im}. In other words, the shear effect is affecting the characteristic exponents since it modifies the natural frequencies of the system. The dimensional frequency spectrum of resonances changes (resonances occur at lower frequency values), but not the dimensionless form of the frequency response charts, which are the same as in Figs. 2, 3, 4, 5, 6, 7, 8 and 9, if the characteristic exponents and the modal damping ratio are the same.

As for the whirl direction, the results displayed in Figs. 2, 3, 4, 5, 6, 7, 8 and 9 are all related to steady-state modal solutions with forward whirl, without backward whirl [47]. The latter would be a consequence of considering non-isotropic supports.

Finally, considering modal superposition, it may happen the case of two, or more resonances of different modes in close proximity of the same frequency, which may produce a magnification, or a reduction of the response amplitude.

5.2 Frequency response analysis, with gyroscopic effects

Even in the presence of non-negligible gyroscopic effect, most conclusions presented in Sect. 4 are still valid. However, some points need further developments and comments, as discussed in the following of this Section, considering the additional difficulty due to the dependency of the characteristic exponents on the external excitation frequency (angular speed).

The steady-state response of the Rayleigh model, described in Eq. (28) is periodic only if:

$$\frac{\hat{\omega}_f}{\hat{\Omega}} = \left(1 - \frac{1}{2}\gamma_n\right)\frac{\omega_U}{\omega_N} = R, \quad R \in \mathbb{Q} \tag{42}$$

that is, only if the frequency of the external load (in the transformed coordinate domain) and the frequency of the parametric excitation are commensurate. However, it should be remembered the inverse coordinate transformation to bring the system back to its original coordinate system. Therefore, the condition of periodicity ($\omega_U / \omega_N = R$) given in Sect. 4, Eq. (36), is still valid even in the presence of gyroscopic effect.

In the case of the Rayleigh model, Eqs. (37) and (38) must be modified considering that in the transformed coordinate domain, the frequency of the external harmonic load is shifted due to gyroscopic effect, and therefore:

$$\frac{\hat{\omega}_f}{\hat{\Omega}} = \left(1 - \frac{1}{2}\gamma_n\right)\frac{\omega_U}{\omega_N} = \pm\hat{\lambda}_{im} + k \; = \hat{\lambda}_k \tag{43}$$

which means that there is a direct effect of the gyroscopic term on the sequence of resonances, consisting of a shift towards higher values of ω_U / ω_N, simply given by a constant (positive) factor dependent on the modal parameter γ_n.

It must be pointed out, however, that there is also another, indirect effect of the same parameter on the sequence in Eq. (43). In fact, the characteristic exponents, and hence λ_{im}, are related to the natural frequency in the transformed coordinate domain ω_{nm}, Eq. (16), which affects the equation of motion according to Eq. (19). Therefore, the sequence of resonances given in Eq. (43) becomes dependent on the angular speed ω_U.

As for the response amplitudes when $a_n \to 0$, the procedure for getting the principal resonance adopted for deriving Eq. (40) can be followed also in this case, yielding:

$$\hat{\omega}_f = 1 \quad \Rightarrow \quad \frac{\hat{\omega}_f}{\hat{\Omega}} = \frac{1}{\hat{\Omega}_0} = \frac{\omega_{nmcr}}{\omega_{N0}} = \mathrm{Im}(\hat{\lambda}) = \hat{\lambda}_{k0} \tag{44}$$

where ω_{nmcr} is the mean natural frequency value at the principal forward critical speed. Because of Eq. (44), and recalling Eq. (16), the principal forward critical speed (say ω_{Ucr}, angular speed at which the principal forward resonance occurs) can be found, together with ω_{nmcr}:

$$\begin{cases} \dfrac{\omega_{Ucr}}{\omega_n} = \dfrac{1}{\sqrt{1-\gamma_n}} \\ \dfrac{\omega_{nmcr}}{\omega_n} = \dfrac{1}{\sqrt{1-\gamma_n}}\left(1 - \dfrac{1}{2}\gamma_n\right) \end{cases} \tag{45}$$

where, as already noted, it must be $\gamma_n < 1$, otherwise no principal forward critical speed can exist (i.e., it tends to infinity as $\gamma_n \to 1$). Note also that the principal forward critical speed tends to be higher than in the case without gyroscopic effect, and that $\omega_{nmcr} \cong \omega_n$ for sufficiently small values of γ_n. As an example, possible values of γ_n for a simply supported iron shaft (density ρ = 7800 kg / m^3, length l = 1 m, hollow circular section with external radius r_e, internal radius r_i) are reported in Fig. 10 (left) for the first 5 modes.

The definition of λ_{im} given in Eq. (40) can now be modified considering the gyroscopic effect:

$$\begin{cases} \hat{\lambda}_{im} = \dfrac{1}{\hat{\Omega}_0} - \mathrm{int}\left(\dfrac{1}{\hat{\Omega}_0}\right) = \dfrac{\omega_{nmcr}}{\omega_{N0}} - \mathrm{int}\left(\dfrac{\omega_{nmcr}}{\omega_{N0}}\right) = \hat{\lambda}_{k0} - \mathrm{int}(\hat{\lambda}_{k0}) \\ \hat{\lambda}_{k0} = \dfrac{\lambda_{k0}}{\sqrt{1-\gamma_n}}\left(1 - \dfrac{1}{2}\gamma_n\right), \;\; \lambda_{k0} = \dfrac{\omega_n}{\omega_{N0}} \end{cases} \tag{46}$$

which is valid at $\omega_U = \omega_{Ucr}$. However, at different values of angular speed ω_U, the definition of λ_{im} changes as a function of ω_U itself, since in this case the angular speed affects the characteristic exponents. Hence, recalling again Eq. (16), Eq. (46) can be generalized as a function of the angular speed ω_U as:

$$\begin{cases} \hat{\lambda}_{im} = \dfrac{\omega_{nm}}{\omega_{N0}} - \mathrm{int}\left(\dfrac{\omega_{nm}}{\omega_{N0}}\right) = \hat{\lambda}_k - \mathrm{int}(\hat{\lambda}_k) \\ \hat{\lambda}_k = \lambda_{k0}\sqrt{1 + \dfrac{\gamma_n^2}{4(1-\gamma_n)}\left(\dfrac{\omega_U}{\omega_{Ucr}}\right)^2}, \quad \lambda_{k0} = \dfrac{\omega_n}{\omega_{N0}} \end{cases} \tag{47}$$

In the presence of a non-negligible gyroscopic effect, the sequence of resonances, which would otherwise be independent on angular speed as in Eqs. (37) and (38), becomes dependent on the gyroscopic modal parameter γ_n and on the angular speed according to Eqs. (43) and (47). In this case, each term of the sequence depends on a different value λ_{im} as a function of ω_U. The sequence of resonances (i.e. the secondary resonances) when $a_n \to 0$ can then

be found by solving the following system, directly descending from Eqs. (43) and (47):

$$\begin{aligned} \hat{\lambda}_k &= \pm\hat{\lambda}_{im} + k \\ \hat{\lambda}_k &= \left(1 - \frac{1}{2}\gamma_n\right)\frac{\omega_U}{\omega_{N0}} = \hat{\lambda}_{k0}\frac{\omega_U}{\omega_{Ucr}} \end{aligned} \tag{48}$$

in which the first equation is an implicit representation of a sequence of curves, each of them being a function of the angular speed ω_U given by Eq. (47), while the second equation is a linear function of ω_U, its angular coefficient given in Eq. (46). Curves and line in Eqs. (47) and (48) are expressed as functions of the dimensionless angular speed ω_U / ω_{Ucr}. The intersection points give the sequence of secondary resonances, as shown in Fig. 10, right, drawn taking $\lambda_{k0} = 11 / 5$ and $\gamma_n = 0.2$. In the case of no gyroscopic effect, the sequence of secondary resonances is determined by knowing just one parameter (λ_{k0}), while in the case of a non-negligible gyroscopic effect, the sequence is determined by setting two parameters (λ_{k0} and γ_n), as shown in Fig. 10, right, in dimensionless form. The first parameter (λ_{k0}) determines the sequence on the vertical axis, at $\omega_U = 0$. The second parameter (γ_n) determines the deviation of each term of the sequence from its value at $\omega_U = 0$.

Once the sequence of resonances when $a_n \to 0$ has been identified in terms of ω_U / ω_{Ucr} (which in Fig. 10, right, is given by normal projection of the intersection points, black dots, on the abscissa axis), it is then possible to get the same sequence in terms of ω / Ω by means of the following linear coordinate transform, descending from Eq. (45):

$$\frac{\omega}{\Omega} = \frac{\hat{\omega}}{\hat{\Omega}} = \frac{\omega_U}{\omega_N} = \frac{1}{\Omega_0\sqrt{1-\gamma_n}}\left(\frac{\omega_U}{\omega_{Ucr}}\right) \tag{49}$$

which allows to draw the maximum amplitude diagram as a function of the ratio ω / Ω as in Figs. 2, 3 and 4, 7, 8 and 9, and therefore to compare on the same diagram the results of the Rayleigh model with those of the Euler–Bernoulli one. Note that in Eq. (49) the ratio $\delta = 1 / \Omega_0$ identifies the initialization point of the principal resonance on the abscissa axis of the Ince-Strutt diagram, as shown in Figs. 2 and 4.

As an example, Fig. 11 shows a comparison of the maximum amplitude diagram already displayed in in Fig. 8, right (black curve: $\gamma_n = 0$, $\zeta_n = 0.03$, $\lambda_{im} = 0.2418$, $\Omega_0 \cong 4/7$) with a diagram obtained using the same input parameters and considering in addition the gyroscopic effect (grey curve; $\gamma_n = 0.15$).

In Fig. 11, the frequency response with gyroscopic effect has been computed by means of Eq. (30), while the theoretical sequence of resonances (vertical dotted lines, undamped case) has been determined by solving the system in Eq. (48). The analytical tool developed in this Section, Eqs. (47) and (48), is able to identify the resonance frequencies of the undamped system when its characteristic exponents depend on both the parametric and external excitation frequencies. Frequency shifts of resonance peaks can be observed, due to gyroscopic effect, following a pattern similar to the one that is possible to deduce from Fig. 10, right. Note that this pattern is not given by a simple proportionality constant, as already discussed. Note also the differences in the hierarchy of peak prominences, which confirms that their dependency on the parametric excitation amplitude α_n and on the modal damping ratio ζ_n is not straightforward, in this case with an additional influence given by the gyroscopic parameter γ_n.

It is important to point out that in the case of the undamped Rayleigh model represented in the transformed coordinates, the Ince-Strutt diagram computed at a fixed value of angular speed retains the same shape as that shown in Figs. 2, 4, 7, 8, and 9 (with tips of the Arnold tongues on the abscissa axis), drawn for the Euler Bernoulli model, or the Euler Bernoulli model plus shear [32]. However, back to the original coordinate system, the Ince-Strutt diagram would appear substantially different, with shifts and merging of Arnold tongues created by combination parametric resonances [35, 36].

In conclusion, gyroscopic effects can produce substantial changes in the dimensionless Mathieu-Hill equation and therefore in the related frequency response charts, mainly consisting of shifting of the resonance peaks at higher (forward) frequency values. The magnitude of these shifts tends to increase with the angular speed, it depends on the modal parameter γ_n, and it cannot be disregarded even for relatively small values of γ_n (see Fig. 10, left).

5.3 Frequency response analysis, varying both excitation frequencies with fixed relative ratio

Some more insights and comments are needed in the case in which the parametric excitation frequency varies proportionally to the angular speed according to a fixed relative ratio, i.e.:

$$\omega_N = p\,\omega_U \tag{50}$$

Indeed, a rather common circumstance in applications, when p is an integer factor. In particular, this is relevant in the case of anisotropy in the rotating elements, and in the presence of cracks [22, 25, 26].

For simplicity, this particular occurrence is discussed in the case of no (or negligible) gyroscopic effect.

If $R = 1 / p$, rational, according to Eq. (36) the response is periodic. Introducing Eq. (50) in Eq. (40) immediately yields the values for λ_{k0} and λ_{im} as functions of p:

$$\lambda_{k0} = \frac{1}{p}, \quad \lambda_{im} = \frac{1}{p} - \text{int}\left(\frac{1}{p}\right), \quad p = 1, 2, \ldots \tag{51}$$

Therefore, as already noted in Sect. 4, point 10, the principal resonance occurs at $R = 1 / p$. Then, as a consequence of Eq. (41), the whole sequence of resonances as $\alpha_n \to 0$ can be expressed either as a function of δ (i.e. ω_n / ω_N, abscissa of the Ince-Strutt diagram) or as a function of ω_n / ω_U, according to:

$$\begin{aligned} p=1 \;&\Rightarrow\; \left.\frac{\omega_n}{\omega_U}\right|_{cr} = \delta_{kcr} = k, \;\; k = 1,2,\ldots \\ p\geq 2 \;&\Rightarrow\; \left.\frac{\omega_n}{\omega_U}\right|_{cr} = p\,\delta_{kcr} = \pm 1 + pk > 0, \;\; k = 1,2,\ldots \end{aligned} \tag{52}$$

At this stage it is also possible to provide a satisfactory explanation to some partial results found in the literature. As an example, the sequence of resonances in the frequency response of the linearized model presented in [6], related to wind turbine dynamics, can be immediately obtained setting $p = 1$. Note that in [6] the frequency response is displayed as a function of the ratio between excitation frequency and natural frequency, hence the sequence of resonances is given by $1 / k$, and also that the amplitude of the response, differently from the present study, is not multiplied by a factor ω^2. In [6], only the super harmonics of order 2 and 3 (occurring at 1/2 and 1/3) are identified, using the method of multiple scales. However, in the frequency response obtained by numerical solution of the linearized problem, it can also be seen the contribution of the super harmonic of order 4 (occurring at 1/4), fourth term of a theoretically infinite sequence.

Finally, as a possible contribution in the field of damage detection in rotors parametrically excited by cracks [26, 48, 49], it should be noted that even in stable operating conditions, the onset of some secondary resonances as in Eq. (52) may provide helpful insights into fault identification procedures.

6 Conclusions

A contribution has been given to highlight fundamental aspects of the steady-state response of asymptotically stable dynamic systems with both parametric and external excitations, making further investigations and results possible also in the field of nonlinear dynamics.

The proposed method has been applied to the analysis of slender rotors with parametric excitation and unbalance, also including shear deformation and gyroscopic effects, but it may also be easily applied to investigate a large variety of dynamic systems in different engineering branches.

The results can be summarized as follows:

1. The steady-state response is aperiodic unless the parametric excitation frequency and the external excitation frequency (angular speed) are commensurate.
2. The frequency components of the response are determined by the governing parameters and by the characteristic exponents of the homogeneous equations of the parametrically excited system.
3. Each modal coordinate of the decoupled system is related to a theoretically infinite sequence of resonances, due to the combination of parametric and external excitation frequencies, for which analytical expressions have been derived, also considering the case in which the characteristic exponents are dependent on the external excitation frequency (angular speed).
4. Flexural critical speeds can occur at lower values than in the same, non-parametrically excited, rotors.

5. Flexural critical speeds tend to increase with gyroscopic effects.
6. The amplitudes of the steady-state response in resonant conditions are highly dependent on the parametric excitation, other than on external damping and (if non-negligible) gyroscopic effect.

Consequently, a correlation has been found between resonances and working points in Ince-Strutt stability maps, introducing a new representation of the frequency responses in the presence of both parametric and non-homogeneous harmonic terms.

The developed analysis, through the dynamic signature given by secondary resonances, can provide a helpful contribution in the field of damage detection, when parametric excitation is generated by wear or damage, as in rotors parametrically excited by cracks, and when the dynamic system is still operating well into stable working conditions.

As a future work, the analysis shall be extended to generalize the results to periodic excitations given by Fourier series expansions, and to consider the effect of anisotropy in the supports on frequency responses, and on whirl behaviour.

Acknowledgements This work was supported by the University of Modena and Reggio Emilia, Department of Engineering Enzo Ferrari, Project FARD 2024 (Grant code FAR_DIP_2024_DIEF-DEFELICE). Part of the results will be presented at the Fourth International Nonlinear Dynamics Conference (NODYCON 2025), Stevens Institute of Technology, Hoboken, NJ, USA, June 22—25, 2025.

Author contributions A.D.F. and S.S. wrote the main manuscript text and A.D.F. prepared all figures. All authors reviewed the manuscript.

Funding Open access funding provided by Università degli Studi di Modena e Reggio Emilia within the CRUI-CARE Agreement. University of Modena and Reggio Emilia, Italy, FAR_DIP_2024_DIEF-DEFELICE.

Data availability No datasets were generated or analysed during the current study.

Declarations

Competing interests The authors declare no competing interests.

Appendix

The equations of motion of the Rayleigh spinning shaft in real coordinates reads [41]:

$$\begin{cases} \rho A\ddot{v}-\rho I\dot{v}^{\mathrm{II}}-\rho J\omega_U\dot{w}^{\mathrm{II}}+EIv^{\mathrm{IV}}-\Delta N\cos(\omega_N t)v^{\mathrm{II}}=f_y \\ \rho A\ddot{w}-\rho I\ddot{w}^{\mathrm{II}}+\rho J\omega_U\dot{v}^{\mathrm{II}}+EIw^{\mathrm{IV}}-\Delta N\cos(\omega_N t)w^{\mathrm{II}}=f_z \end{cases} \tag{53}$$

Decoupling the partial differential equations, as for instance in the case of simply supported ends:

$$\begin{Bmatrix} v_n \\ w_n \end{Bmatrix} = \sin\left(\frac{n\pi x}{l}\right)\begin{Bmatrix} \eta_n(t) \\ \mu_n(t) \end{Bmatrix} \tag{54}$$

and disregarding the parametric excitation ($\Delta N = 0$), yields the following system of two modal ordinary differential equations:

$$\begin{cases} \ddot{\eta}_n+\gamma_n\omega\,\dot{\mu}_n+\omega_n^2\eta_n=f_{yn} \\ \ddot{\mu}_n-\gamma_n\omega\,\dot{\eta}_n+\omega_n^2\mu_n=f_{zn} \end{cases} \tag{55}$$

which can be reduced to a single fourth-order ordinary differential equation:

$$\ddot{\ddot{\eta}}_n+\left[2\omega_n^2+(\gamma_n\omega)^2\right]\ddot{\eta}_n+\omega_n^4\eta_n=\ddot{f}_{yn}-\gamma_n\omega\dot{f}_{zn}+\omega_n^2 f_{yn} \tag{56}$$

with characteristc equation given by:

$$s^4+\left[2\omega_n^2+(\gamma_n\omega)^2\right]s^2+\omega_n^4=0 \tag{57}$$

yielding the same four roots as in Eq. (15).

References

1. Smith, J.J.: A method of solving Mathieu's equation. Trans. Am. Inst. Elect. Eng., Part I: Commun. and Electron. **74**(4), 520–525 (1955)
2. Barrow, W.L., Smith, D.B., Baumann, F.W.: A further study of oscillatory circuits having periodically varying coefficients. J. Franklin Inst. **221**(4), 509–529 (1936)
3. D'Angelo, H.: Linear Time Varying Systems: Analysis and Synthesis. Allyn and Bacon, Boston (1970)
4. Yakubovich, V.A., Starzhinskii, V.M.: Linear differential equations with periodic coefficients. Parts I and II. Wiley, New York (1975)
5. Richards, J.A.: Analysis of periodically time-varying systems. Springer, New York (1983)
6. Ramakrishnan, V., Feeny, B.F.: Resonances of a forced Mathieu equation with reference to wind turbine blades. J. Vib. Acous. **134**(6), 64501 (2012)
7. Dupal, J., Zajicek, M.: Existence of analytical solution, stability assessment and periodic response of vibrating systems with time varying parameters. Appl. Comput. Mech. **14**, 123–144 (2020)
8. Shadman, D., Mehri, B.: A non-homogeneous Hills equation. Appl. Math. Comput. **167**, 68–75 (2005)
9. Rodriguez, A., Collado, J.: Periodic solutions in non-homogeneous Hill equation. Nonlinear Dyn. Syst Theory **20**(1), 78–91 (2020)
10. Kwong, M.K., Wong, J.S.W.: On the oscillation of Hill's equations under periodic forcing. J. Math. Anal. Appl. **320**, 37–55 (2006)
11. Zhou, Z.: Subharmonic solutions of Hill's equation. Appl. Math. Comput. **253**, 17–22 (2015)
12. Jazar, G.N.: Stability chart of parametric vibrating systems using energy-rate method. Int. J. Non-Linear Mech. **39**, 1319–1331 (2004)
13. Bolotin, V.V.: The dynamic stability of elastic systems. Holden-Day, San Francisco (1964)
14. Bolotin, V.V.: Non-conservative problems of the theory of elastic stability. The MacMillan Company, New York (1963)
15. Chen, L.W., Ku, D.M.: Dynamic stability analysis of a rotating shaft by the finite element method. J. Sound Vib. **143**(1), 143–151 (1990)
16. Lee, H.P.: Effects of axial base excitations on the dynamic stability of spinning pre-twisted beams. J. Sound Vib. **185**(2), 265–278 (1995)
17. Bauchau, O.A., Nikishkov, Y.G.: An implicit Floquet analysis for rotorcraft stability evaluation. J. Am. Helicopter Soc. **46**, 200–209 (2001)
18. Anilkumar, A., Kartik, V.: In-plane vibration of a rigid body attached to a flexible rotating beam". J. Sound and Vib. **475**, 115245 (2020)
19. Tentarelli, M., Cantelli, S., De Felice, A., Sorrentino, S.: Parametric excitation as a cause of clutch judder: theoretical study and experimental validation. Mech. Syst. and Signal Process. **193**, 110256 (2023)
20. Smith, D.M.: The motion of a rotor carried by a flexible shaft in flexible bearings. Proceed. Royal Soc. Series A **142**, 92–118 (1933)
21. Dimentberg, F.M.: Flexural Vibrations of Rotating Shafts. Butterworth, London (1961)
22. Penny, J.E.T., Friswell, M.I.: The dynamics of rotating machines with cracks. Mater. Sci. Forum **440–441**, 311–320 (2003)
23. Ricci, R., Pennacchi, P.: Discussion of the dynamic stability of a multi-degree-of-freedom rotor system affected by a transverse crack. Mech. Mach. Theory **58**, 82–100 (2012)
24. Sinha, S.K.: On general conditions of rotordynamic stability under combined axial force and torque. Trans. ASME J. Appl. Mech. **59**(1), 225–228 (1992)
25. Al-Shudeifat, M.A.: Stability analysis and backward whirl investigation of cracked rotors with time-varying stiffness. J. Sound Vib. **348**, 365–380 (2015)
26. Kulesza, Z., Sawicki, J.T.: Damping by parametric excitation in a set of reduced-order cracked rotor systems. J. Sound Vib. **354**, 167–179 (2015)
27. Wettergren, H.L., Olsson, K.O.: Dynamic instability of a rotating asymmetric shaft with internal viscous damping supported in anisotropic bearings. J. Sound Vib. **195**(1), 75–84 (1996)
28. Maldonado, D.J.G., Karev, A., Hagedorn, P., Ritto, T.G., Sampaio, R.: Analysis of a rotordynamic system with anisotropy and nonlinearity using the Floquet theory and the method of normal forms. J. Sound Vib. **453**, 201–213 (2019)
29. Wang, S., Wang, Y., Zi, Y., He, Z.: A 3D finite element-based model order reduction method for parametric resonance and whirling analysis of anisotropic rotor-bearing systems. J. Sound Vib. **359**, 116–135 (2015)
30. Oh, J., Palazzolo, A., Hu, L.: Stability of non-axisymmetric rotor and bearing systems modelled with three-dimensional-solid finite elements. J. Vib. Acous. **142**, 011010 (2020)
31. Ishida, Y., Ikeda, T., Yamamoto, T., Esaka, T.: Parametrically excited oscillations of a rotating shaft under a period axial force. JSME Int. J. Series 3, Vib., Control Eng. Eng. for Indus. **31**(4), 698–704 (1988)
32. Raffa, F.A., Vatta, F.: Dynamic instability of axially loaded shafts in the Mathieu map. Meccanica **42**, 347–553 (2007)
33. Yong-Chen, P.: Stability boundaries of a spinning rotor with parametrically excited gyroscopic system. Euro. J. Mech. A / Solids **28**, 891–896 (2008)
34. Mazzei, A.J., Scott, R.A.: Effects of internal viscous damping on the stability of a rotating shaft driven through a universal joint. J. Sound Vib. **265**(4), 863–885 (2003)
35. De Felice, A., Sorrentino, S.: Damping and gyroscopic effects on the stability of parametrically excited continuous rotor systems. Nonlinear Dyn. **103**(4), 3529–3555 (2021)
36. De Felice, A., Sorrentino, S.: Effects of anisotropic supports on the stability of parametrically excited slender rotors. Nonlinear Dyn. **109**(2), 793–813 (2022)
37. Grosso, P., De Felice, A., Sorrentino, S.: A method for the experimental identification of equivalent viscoelastic models from vibration of thin plates. Mech. Syst. and Signal Process. **153**, 107527 (2021)
38. Meirovitch, L.: Principles and techniques of vibrations. Prentice Hall, Upper Saddle River (1997)
39. De Felice, A., Sorrentino, S. "Insights into the gyroscopic behaviour of axially and torsionally loaded rotating shafts". In: Proceedings of the 24th International Conference on Sound and Vibration (ICSV24), London, United Kingdom, July 23–27, 2017: article 879.

40. De Felice, A., Sorrentino, S. "The second spectrum in Timoshenko beam theory: a new approach for its identification." In: Proceedings of 25th International Conference on Sound and Vibration (ICSV25). Hiroshima, Japan, July 8–12, 2018, Vol. 8: pp. 4640–4647.
41. De Felice, A., Sorrentino, S.: On the dynamic behaviour of rotating shafts under combined axial and torsional loads. Meccanica **54**(7), 1029–1055 (2019)
42. Cunningham, W.J.: Introduction to nonlinear analysis. McGraw Hill, New York (1958)
43. Deconinck, B., Kutz, J.N.: Computing spectra of linear operators using the Floquet-Fourier-Hill method. J. Comput. Phys. **219**, 296–321 (2006)
44. Ying, Z.G., Ni, Y.Q., Ko, J.M.: Parametrically excited instability analysis of a cable under two support motions. Int. J. Struct. Stab. Dyn. **06**(01), 43–58 (2006)
45. Ying, Z.G., Ni, Y.Q., Fan, L.: Parametrically excited stability of periodically supported beams under longitudinal harmonic excitations. Int. J. Struct. Stab. Dyn. **19**(09), 1950095 (2019)
46. Arnold, V.I.: Remarks on the perturbation theory for problems of Mathieu type. Russ. Math. Surv. **38**(4), 215–233 (1983)
47. AL-Shudeifat, M.A.: New backward whirl phenomena in intact and cracked rotor systems. J. Sound and Vib. **443**, 124–138 (2019)
48. Bachschmid, N., Pennacchi, P., Tanzi, E.: Cracked Rotors: A Survey on Static and Dynamic Behaviour Including Modelling and Diagnosis. Springer, Berlin (2010)
49. Nasar, R.A., Alzarooni, T., Al-Shudeifat, M.A.: On modeling and damage detection methodologies in rotor systems. Nonlinear Dyn. **112**, 16657–16710 (2024)